Structural Insights into the Interaction of Coronavirus Papain-Like Proteases and Interferon-Stimulated Gene Product 15 from Different Species

Courtney M. Daczkowski [1,†], **John V. Dzimianski** [1,†], **Jozlyn R. Clasman** [2], **Octavia Goodwin** [1], **Andrew D. Mesecar** [2] and **Scott D. Pegan** [1]

1 - Department of Pharmaceutical and Biomedical Sciences, University of Georgia, Athens, GA 30602, USA
2 - Department of Biochemistry, Purdue University, West Lafayette, IN 47907, USA

Correspondence to Scott D. Pegan: College of Pharmacy University of Georgia, 422 Pharmacy South, Athens, GA 30602, USA. spegan@uga.edu, scott.d.pegan@gmail.com
http://dx.doi.org/10.1016/j.jmb.2017.04.011
Edited by M. Guss

Abstract

Severe acute respiratory syndrome coronavirus (SARS-CoV) and Middle East respiratory syndrome coronavirus (MERS-CoV) encode multifunctional papain-like proteases (PLPs) that have the ability to process the viral polyprotein to facilitate RNA replication and antagonize the host innate immune response. The latter function involves reversing the post-translational modification of cellular proteins conjugated with either ubiquitin (Ub) or Ub-like interferon-stimulated gene product 15 (ISG15). Ub is known to be highly conserved among eukaryotes, but surprisingly, ISG15 is highly divergent among animals. The ramifications of this sequence divergence to the recognition of ISG15 by coronavirus PLPs at a structural and biochemical level are poorly understood. Therefore, the activity of PLPs from SARS-CoV, MERS-CoV, and mouse hepatitis virus was evaluated against seven ISG15s originating from an assortment of animal species susceptible, and not, to certain coronavirus infections. Excitingly, our kinetic, thermodynamic, and structural analysis revealed an array of different preferences among PLPs. Included in these studies is the first insight into a coronavirus PLP's interface with ISG15 via SARS-CoV PLpro in complex with the principle binding domain of human ISG15 (hISG15) and mouse ISG15s (mISG15s). The first X-ray structure of the full-length mISG15 protein is also reported and highlights a unique, twisted hinge region of ISG15 that is not conserved in hISG15, suggesting a potential role in differential recognition. Taken together, this new information provides a structural and biochemical understanding of the distinct specificities among coronavirus PLPs observed and addresses a critical gap of how PLPs can interact with ISG15s from a wide variety of species.

© 2017 Elsevier Ltd. All rights reserved.

Introduction

Coronaviruses (CoVs) are enveloped, positive-stranded RNA viruses that cause mild to severe infections in a wide range of mammals and birds. Specifically, severe acute and Middle East respiratory syndrome CoVs (SARS-CoV and MERS-CoV) are well-recognized viral pathogens that have emerged from different animal reservoirs to cause deadly disease in humans. SARS-CoV first emerged in 2002 with a case fatality rate of 10%, claiming the lives of over 800 people and infecting more than 8000 [1,2]. After 10 years, MERS-CoV emerged with a shocking case fatality rate of nearly 35% and has spread to 27 different countries to date [3]. The continuing threat of MERS-CoV was recently under-scored by one of its most recent outbreaks in Republic of Korea. This outbreak quickly led to 36 deaths, which has brought the total MERS-CoV global deaths to over 600 [4,5].

Similar to other positive-stranded RNA viruses, CoVs encode two types of cysteine proteases, including the papain-like protease [(PLP) for viruses that have more than one papain-like protease (PLpro)] and 3C-like protease, also known as the main protease. Together, these enzymes cleave the viral polyprotein into 16 different nonstructural proteins (Nsps 1–16) in order to generate the membrane-bound replicase complex for RNA replication [6–9]. CoVs encode either a single PLP, termed PLpro, or

two PLPs that process a total of three cleavage sites within the polyprotein [7,10]. For instance, SARS-CoV and MERS-CoV encode a single PLpro, while other CoVs such as mouse hepatitis virus (MHV) encode for both the PLP1 and PLP2 (Fig. 1a).

Beyond cleaving the viral polyprotein, PLPs have additional activities that promote virus replication.

The X-ray structure of the first CoV PLP determined from SARS revealed that these enzymes resemble the structure of human ubiquitin (Ub)-specific proteases (USPs) and are thereby known as viral USPs, often acting as deubiquitinating enzymes (DUBs) with the ability to remove the post-translational modification Ub from target proteins [8]. Some PLPs are also
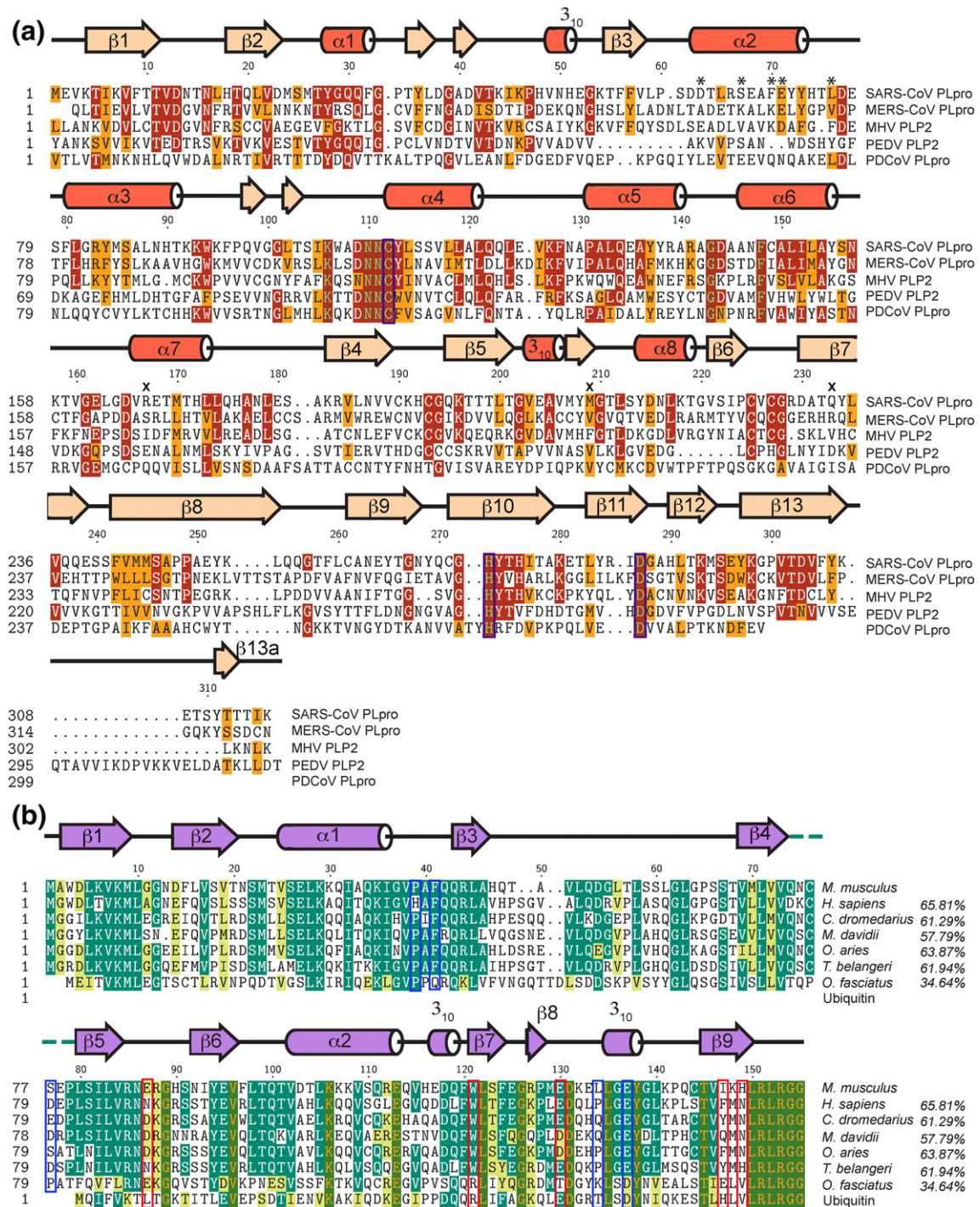

Fig. 1 (*legend on next page*)

deISGylating enzymes with the ability to reverse the post-translational modification of the Ub-like (Ubl) protein interferon-stimulated gene product 15 (ISG15) from cellular proteins [11]. Such activities were implicated in SARS-CoV's suppression of the innate immune responses, particularly antagonizing type-I interferon (IFN) signaling and chemokine and cytokine production [12,13]. Simultaneous disruption of both activities, either by mutation in MERS CoV PLpro's Ub/Ubl binding region [14] or by a destabilizing mutation in MHV PLP's Ubl domain [10], has been observed to prevent the antagonization of IFN signaling, chemokine and cytokine production, and viral pathogenesis, respectively. Overall, these studies suggest that the deubiquitinating and deISGylating activities of PLPs, sometimes packaged together as DUB activity, are a likely contributor to viral pathogenesis.

Intriguingly, the precise role of each individual activity in promoting PLPs' ability to act as an IFN antagonist has yet to be precisely defined. So far, several X-ray structures of PLpro and PLP2 bound with Ub molecules have been reported [8,15,16]. However, no structure of any CoV PLP in complex with an ISG15 molecule has yet been reported. Due to the lack of structural detail about the interface between CoV PLPs and ISG15, understanding how CoVs' PLPs specifically engage with ISG15s *versus* Ub has been especially difficult to understand. The lack of structural information has led to problems in defining the differences between CoV PLPs' deubiquitinating and deISGylating activities among different CoVs. A further complication in our understanding stems from the fact that the sequence identity of ISG15 among mammals is low, ranging from 58% to as low as 35% when a broader range of animals is compared (Fig. 1b). In contrast, Ub is highly conserved among eukaryotes.

The sequence diversity of ISG15 among animals and the impact of this diversity on the recognition of these ISG15s by viral USPs have not been well studied despite the potential implications. For example, certain CoVs, such as SARS-CoV and MERS-CoV, are known to replicate and survive in a broad range of animals including bats, camels, mice, civets, shrews, badgers, pigs, and humans [10,17,18]. In contrast, other CoVs such as MHV only replicate in mice, suggesting that some CoV PLPs may have evolved strict specificity for their single host's ISG15 [19]. The potential for species–species variances in ISG15 has already been shown to be a key factor in other viruses including influenza B where it was shown that NS1 is unable to bind mouse ISG15 (mISG15) unlike its non-human primate and human counterparts, limiting influenza B virus infection in mice [20–22]. Also, biodiversity that occurs between species within ISG15s was recently shown to impact the ability of nairovirus viral ovarian tumor domain proteases (vOTUs) to effectively process certain ISG15s [23]. Overall, many CoV PLPs have been observed to show robust deubiquitinating activities; [11,24] however, recent *in vivo* studies have started to unveil the importance of PLPs deISGylating activity [25,26]. This has led to a need for a better and more detailed understanding of the interactions between CoV PLPs and ISG15 at the molecular level.

Adding to the ambiguity of how CoV PLPs or other deISGylating enzymes interact with ISG15, especially when it comes to understanding species-to-species variations, is the lack of available full-length ISG15 structures that have been determined. This is especially important when the intramolecular arrangement of the two domains of ISG15 is considered. For example, the hinge region of ISG15 shows a significant degree of sequence diversity between the different species (Fig. 1b). Although several structures of human ISG15 (hISG15) have been reported, no complete structure of ISG15 from another species has been resolved. Moreover, the recent elucidation of the structure of the C-terminal domain portion of mISG15 prompted questions on the impact of ISG15 biodiversity on the overall ISG15 structural fold [23].

To address these critical gaps in our understanding of ISG15 recognition by CoV PLPs, PLpro from SARS-CoV and MERS-CoV, and PLP2 from MHV were examined for differences in their selectivity among ISG15s from various animals. The X-ray crystal structures of SARS-CoV PLpro bound to the C-terminal domain of ISG15 originating from mouse and human

Fig. 1. (a) The PLPs from SARS CoV (accession number: P0C6U8), MERS CoV (accession number: AFS88944.1), MHV (accession number: P0C6V0), PEDV (accession number: AKP80587.1), and Porcine deltacoronavirus (PDCoV; accession number: AHM88399.1). The sequence numbering ruler is based on the SARS-CoV PLpro sequence. Residues forming the catalytic triad are boxed in purple. The secondary structure of SARS-CoV PLpro based on DSSP is denoted, with α- and 3_{10}-helices in reddish orange and β-sheets in wheat. Residues forming the "ridge" of SARS-CoV PLpro are marked with an asterisk (*). Residues of SARS-CoV PLpro mutated in this study are denoted ("x"). (b) Sequence alignment of ISG15s from mouse (*Mus musculus*, accession number: AAB02697.1), human (*Homo sapiens*, accession number: AAH09507.1), dromedary camel (*Camelus dromedarius*, accession number: XP_010997700.1), vesper bat (*Myotis davidii*, accession number: ELK23605.1), sheep (*Ovis aries*, accession number: AF152103.1), northern tree shrew (*Tupaia belangeri*, accession number: AFH66859.1), and jackknife fish (*Oplegnathus fasciatus*, accession number: BAJ16365.1) along with ubiquitin. The sequence numbering ruler is based on mouse ISG15 (mISG15). Secondary structure of mISG15 based on DSSP is denoted in purple. The hinge region between β4 and β5 is denoted using a dashed line in teal. Percentages indicate sequence identity relative to mISG15. Residue positions identified in this study that form key interactions with SARS-CoV PLpro are boxed in red. Residue positions implicated in driving the specific tertiary fold features of mouse and human ISG15 are boxed in blue.

were determined and analyzed in conjunction with enzyme kinetic and thermodynamic data derived from isothermal titration calorimetry (ITC). In addition, the first X-ray structure of a complete non-hISG15 structure, mISG15, was also determined to elucidate the potential sequence and structural differences that may account for species specificity of CoV PLPs. Together, these studies provide significant and new insight into the CoV PLP's ability to accommodate the structural differences not only between Ub and hISG15 but also in different species' ISG15s.

Results

Species-specific cleavage of proISG15s by CoV PLPs

Currently, there is a paucity of available biochemical data on the impact of species-to-species sequence variations within ISG15 and the effect that these differences may have on the ability of CoV PLPs to recognize and cleave ISG15. Therefore, we employed a recently developed assay for deISGylating vOTUs that takes advantage of the ability of a protease or DUB to cleave immature ISG15 [23]. The PLpro enzymes from SARS-CoV and MERS-CoV, and the enzyme PLP2 from MHV, were purified and assessed for their ability to cleave proISG15s derived from seven different species including human, sheep, northern tree shrew, jackknife fish, mouse, dromedary camel, and vesper bat (Fig. 2). Each of these proISG15 proteins is appended with the proISG15 extension from *Homo sapiens* (Fig. 2). ISG15 from jackknife fish was included in the analysis to add a more distantly related ISG15 homolog.

SARS-CoV and MERS-CoV PLpros are both capable of fully processing proISG15 from human, mouse, camel, and bat within 60 min. SARS PLpro is also able to fully process proISG15 from sheep and shrew within that same time, but it has little to no activity
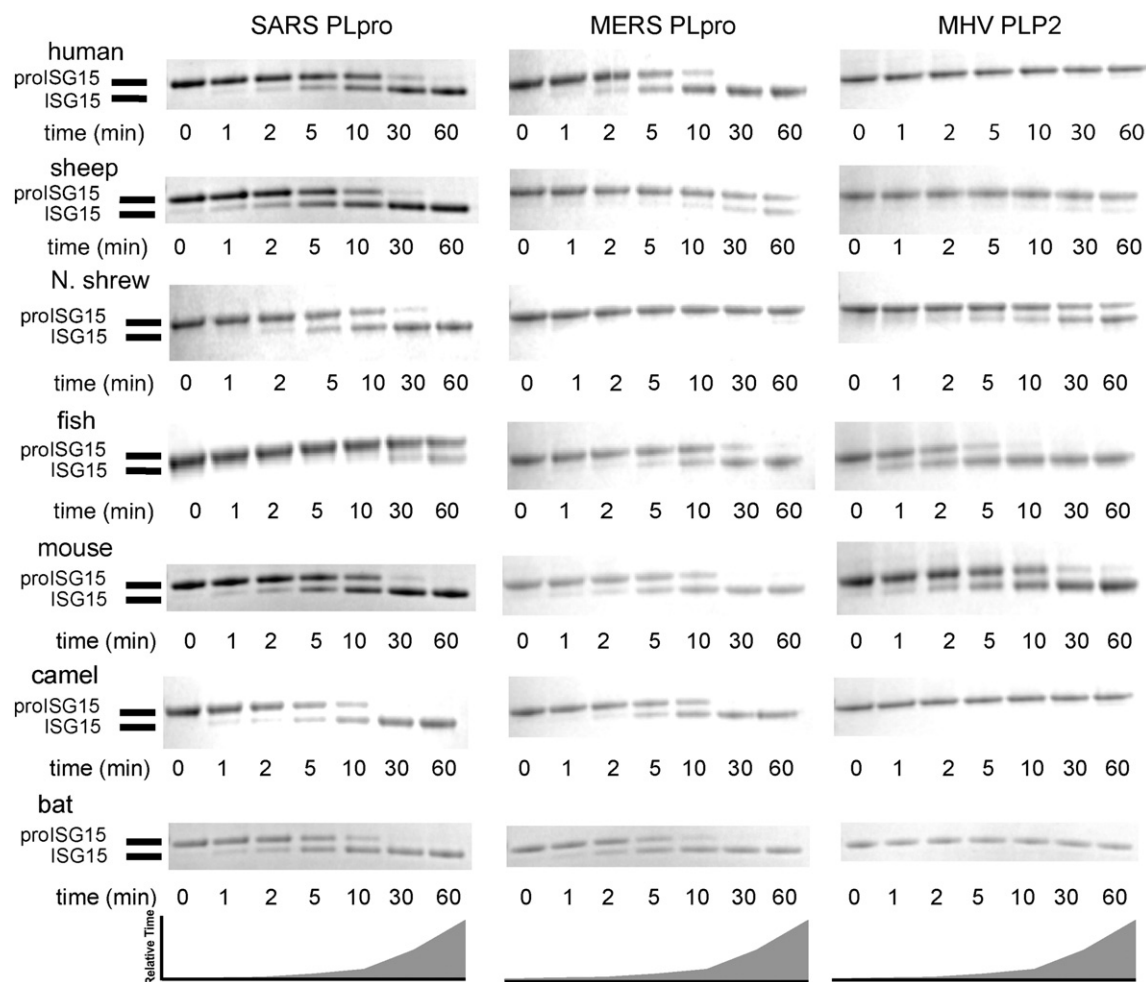
Fig. 2. Cleavage profiles of SARS-CoV PLpro, MERS-CoV PLpro, and MHV PLP2 with proISG15s derived from human, sheep, northern tree shrew, jackknife fish, mouse, dromedary camel, and vesper bat. Reactions were conducted at 37 °C with 10 μM of each proISG15 and 20 nM of each PLpro/PLP2 with samples taken at the indicated time points.
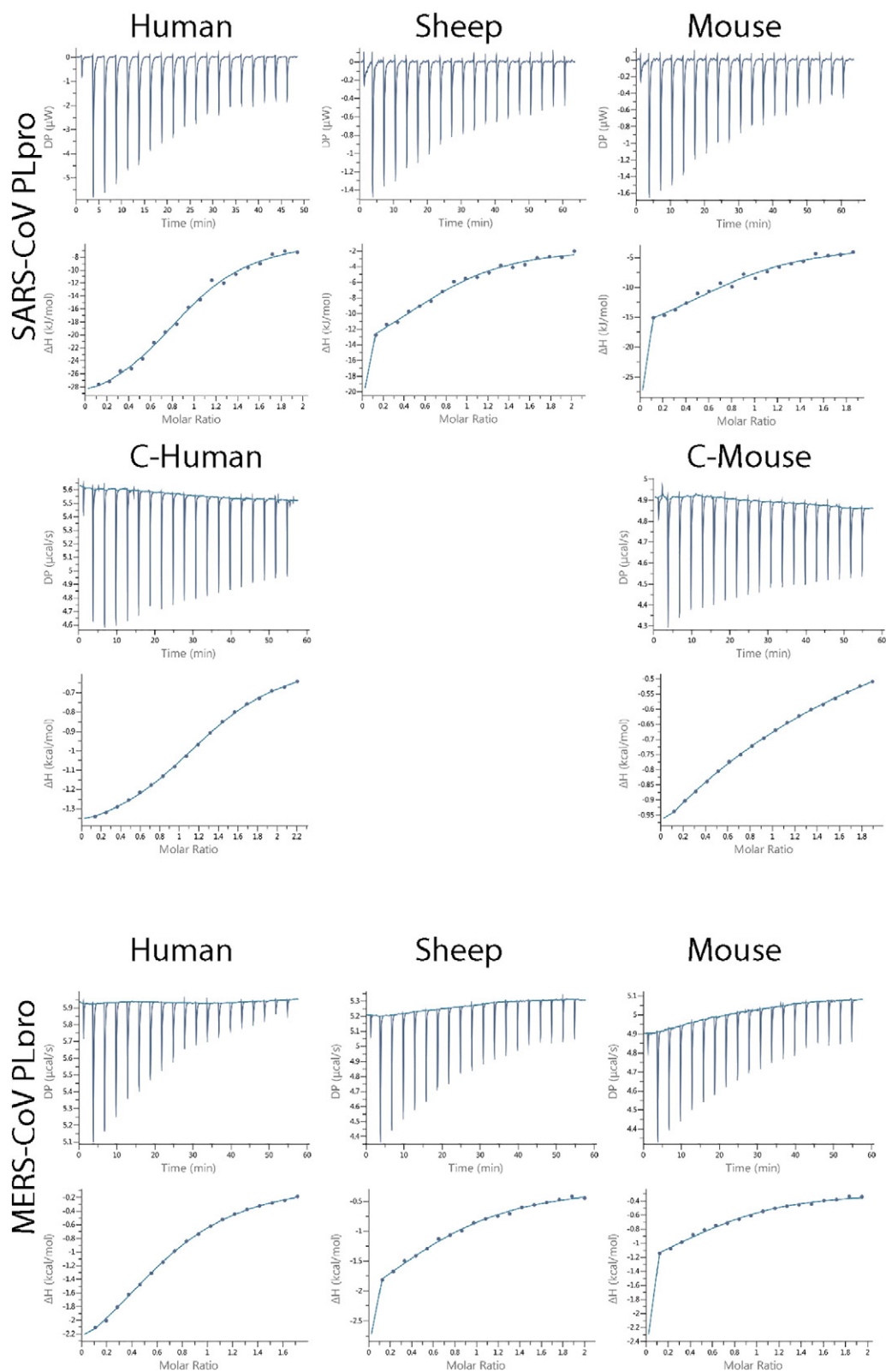
Fig. 3. ITC binding isotherms with the raw heat (top panel) and the integrated heats of injection (bottom panel) shown for each interaction.

against jackfish proISG15. In contrast, MERS PLpro is fully capable of processing jackfish proISG15, but it processes proISG15 from shrew and sheep poorly. MHV PLP2, on the other hand, displays a much

narrower specificity for ISG15s from different species. It shows little to no cleavage of proISG15s derived from human, sheep, camel, or bat sources but does show modest activity for the northern tree shrew. MHV

Fig. 4 (*legend on next page*)

PLP2 shows strong activity toward jackfish and mouse proISG15, the latter activity being consistent with MHV's pathogenicity as a murine CoV.
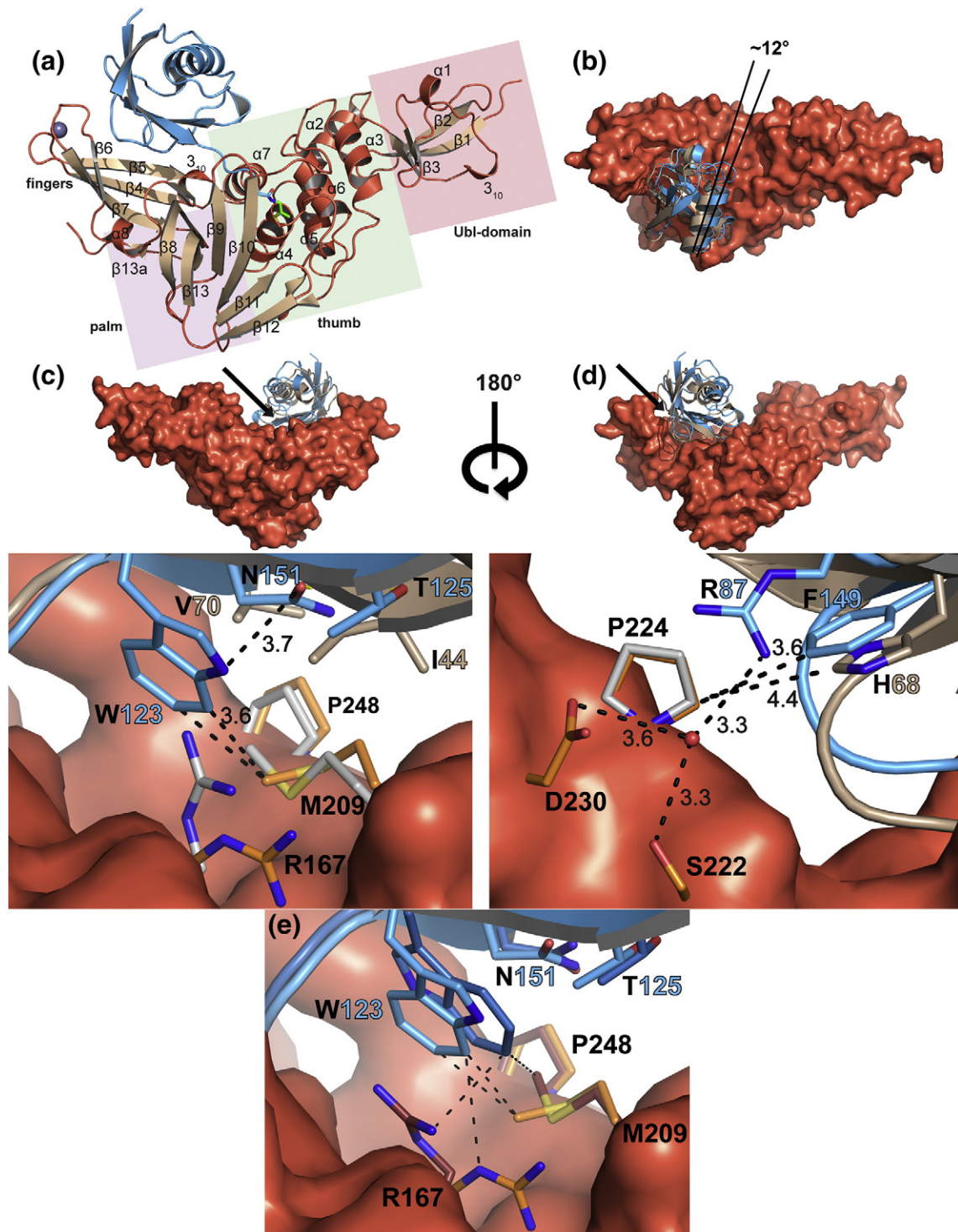
Species specific affinity of ISG15 for SARS-CoV and MERS-CoV PLpros

Analysis of the cleavage patterns in Fig. 2 suggests that SARS and MERS PLpros are more promiscuous in recognizing and cleaving various proISG15s compared to MHV PLP2, which may relate to the fact that these human pathogens are capable of replicating in different hosts, for example, bats, camels, and the shrew, in contrast to MHV that can only replicate in the mouse. Differences in cleaving ability of proISG15s by SARS and MERS PLpro may be due to sequence and structural differences, which may affect binding affinities for the ISG15s. This possibility was explored using ITC to measure the binding affinities of different ISG15s missing the P′-sites (Fig. 3). As deISGylases natural substrates include an isopetide bond, removal of the P′-sites also allows the avoidance of potential confounding factors related to CoV PLPs' other prominent function of processing the viral polyprotein to promote viral replication. This part of the process requires that PLPs recognize and cleave the peptide bond after the LXGG sequences within the polyprotein, and the ability of PLPs to cleave this bond has been shown to be reliant on residues flanking the peptide cleavage site [6,9]. This requisite function is not associated with other viral deISGylating proteases such as nairovirus vOTUs [23]. Therefore, ITC measurements were performed using mature ISG15. Although the mature ISG15s resemble the product by the absence of an isopetide bond, binding affinity could be assessed independent of any P′-sites contribution associated with using the ISG15-pro-form protein. This would also provide a more quantitative understanding of the thermodynamic parameters related solely to the species and virus-related variances of the protease and ISG15s, respectively.

Intriguingly, both SARS-CoV and MERS-CoV PLpro have stronger affinity toward hISG15 than shISG15 and mISG15. The dissociation constants (K_d) of SARS-CoV and MERS-CoV PLpro for hISG15 are 20.5 ± 4.5 μM and 59.3 ± 4.5 μM, respectively. Unlike their affinities for hISG15, the affinities of both PLpros for shISG15 and mISG15 were significantly weaker, and as a result, a competitive ITC binding assay (Table 2 and Fig. 3) had to be used to determine their K_d values. In regard to SARS-CoV PLpro, ITC analyses revealed similar K_d's of 200 ± 41 μM and 198 ± 64 μM for shISG15 and mISG15. More divergence in affinity for mISG15 and shISG15 were seen with MERS-CoV PLpro. Like SARS-CoV PLpro, affinity of MERS-CoV PLpro for shISG15 was similar with a K_d of 147 ± 36 μM. However, a substantially weaker affinity of MERS-CoV PLpro for mISG15 was observed (K_d of 376 ± 53 μM).

The measured thermodynamic parameters revealed that both SARS-CoV and MERS-CoV PLpro follow a similar trend and prefer hISG15 over shISG15 and mISG15. Specifically, the association of shISG15 and mISG15 to PLpros is unfavorable with increasingly higher entropic factors. Although PLpros originating from MERS-CoV and SARS-CoV exhibited a similar preference for hISG15, the thermodynamics driving the affinity differ. The SARS-CoV and hISG15 binding event was driven by enthalpic factors and was slightly entropically unfavorable. In contrast, the MERS-CoV affinity of hISG15 was more balanced, possessing an entropic and enthalpic component.

Although some DUB proteases that possess deISGylating activity have been observed to engage only the C-terminal domain of ISG15, SARS-CoV has been suggested to interact with both domains [11,15,23,27]. To gain insight into the relative contributions of the C-terminal domain to their full-length counterparts, we performed ITC, utilizing both mouse and human C-terminal variants of ISG15. The K_d of 57.6 ± 3.21 μM was observed for ChSIG15. Although the binding event still was enthalpically favorable, this

Fig. 4. (a) Cartoon representation of the SARS-CoV PLpro complexed with ChISG15 (blue). Secondary structure of the PLpro is designated, with helices and loops rendered in reddish orange and β-sheets rendered in wheat. The structural domains of the PLpro are identified, consisting of the fingers (white), palm (purple), thumb (green), and Ubl (red) labeled with colored boxes. The vinyl thioether propargylamine linker is colored green, and the Zn(II) ion in light purple. (b) Overlay of ChISG15 (blue) bound to SARS PLpro (reddish orange) compared to a Ub (light brown)-bound structure (PDB entry: 4MM3) based on a secondary structure alignment of the respective PLpros. The approximate degree of shift in the orientation of analogous α-helices is indicated. (c) Comparison of the interaction of ChISG15 (blue) *versus* Ub (light brown) with the hydrophobic patch of SARS-CoV PLpro, with the site of interaction within the overall structure indicated by an arrow. Side-chain conformations of the PLpro are colored orange for the ChISG15-bound structure, gray for the Ub-bound structure. Residues E127–D133 of ChISG15 and A46–T55 of Ub were removed for clarity. Inter- and intramolecular distances (Å) are shown by black dashes. (d) Comparison of ChISG15 *versus* Ub at the site of the additional hydrophobic interaction in the ChISG15-bound structure. Colored as in (c). Intermolecular distances (Å) are shown as as black dashes. (e) Interchain variability of ChISG15 Trp123 in binding to SARS-CoV PLpro. The two copies within the asymmetric unit were overlaid based on a secondary structure alignment of the PLpros. Side chains of the PLpro colored in orange correspond to the ChISG15 colored light blue, and the PLpro side chains colored burgundy to the ChISG15 colored a darker blue. Intermolecular distances are colored in black. Residues E127–D133 of ChISG15 are omitted for clarity.

contribution was fourfold less than that observed for hISG15. Conversely, it possessed a markedly favorable entropic component over the slightly disfavorable one of its full-length counterpart. Not unsurprisingly, the trend of SARS-CoV having a stronger affinity toward hISG15 over mISG15 was also observed in the C-terminal domain of each substrate. The K_d for C-terminal domain of ISG15 from mouse (CmISG15) was considerably weak at 1870 ± 173 μM, showing marked decreases in both entropic and enthalphic binding contributions and suggesting that similar to hISG15, mISG15's N-terminal domain may also be involved in the protease–ISG15 binding interface.

Crystallization of SARS-CoV PLpro bound to the C-terminal domains of hISG15 and mISG15

While X-ray crystal structures have been solved for SARS and MERS PLpro bound to Ub, our understanding of the interactions of these enzymes with ISG15 has been largely limited to enzymatic, mutational, and computational modeling studies [11,15]. To gain molecular insight into the specific interactions between PLPs and ISG15, we crystallized and determined the X-ray structures of SARS PLpro bound to the C-terminal domains of ISG15, ChISG15 and CmISG15. Attempts at co-crystallization of full-length ISG15s from human and other species with SARS CoV PLpro, as either various covalent adducts or non-covalently bound species, were made but were unsuccessful. However, the complex of SARS-CoV PLpro bound to the ChISG15, which is the principle binding domain of ISG15, crystallized readily [11]. Specifically, we utilized a form of ChISG15 and CmISG15 that were modified with propargylamine at the C terminus (ChISG15-PA or CmISG15-PA) to form a suicide substrate that covalently links to the active site cysteine. From here on in, these covalently modified complexes of SARS PLpro are designated as SARS-CoV PLpro–ChISG15 and SARS-CoV PLpro–CmISG15 for simplicity.

X-ray SARS-CoV PLpro bound to the C-terminal domain of hISG15

The X-ray structure of the SARS-CoV PLpro–ChISG15 complex was determined to 2.62 Å with two complete copies of SARS-CoV PLpro–ChISG15 within the asymmetric unit (Table 3). The structure of CoV PLPs contains the classic tertiary fold associated with PLPs consisting of the finger, palm, thumb, and Ubl domains (Fig. 4a). However, despite sharing the same tertiary fold, the manner in which SARS-CoV PLpro engages the C-terminal domain of hISG15 is distinct from that of Ub. Overlaying the SARS-CoV PLpro–ChISG15 structure with the structure of SARS-CoV PLpro with mono-Ub (PDB entry: 4MM3) reveals that compared to Ub, ChISG15 is shifted by approximately 12° in its global orientation (Fig. 4b).

Closer examination of the binding interface uncovered key differences in how each substrate engages the surface of the SARS-CoV PLpro. Although there is only a minor variation surrounding a 180° flip of Trp123 between the two copies of ChISG15 in the asymmetric unit, both ChISG15 chains are analogous in how they are accommodated by SARS-CoV PLpro compared to Ub (Fig. 4e). The differences appear to be driven by how hISG15 and Ub differ in their ability to interact with a hydrophobic region consisting of residues Arg167, Met209, and Pro248. For Ub, the interactions with this region occur by means of a hydrophobic patch consisting of Ile44, Val70, and Leu8 [15]. In contrast, ISG15 lacks such a hydrophobic patch. The interaction is primarily driven by two distinct sets of hydrophobic interactions: hISG15's Trp123 with Met209 of the protease's palm region, and hISG15's Phe149 with a second hydrophobic site driven by Pro224 of the protease's fingers region (Fig. 4c and d). This predominate hydrophobic binding nature was also seen in the ITC results of SARS-CoV with ChSIG15, with an observed increase in entropic favorable interactions when compared with the hISG15 (Table 2). Surprisingly, while the Ub-bound structure contains other polar and water-mediated interactions between Ub and the palm region of the PLpro, such interactions seem to be less pronounced in the more charged ChISG15 structure [15]. Overall, there are only a few water molecules present within the interface between PLpro and ChISG15 compared to the larger number that is observed in the Ub-bound structure, potentially indicating a lesser role of water-mediated hydrogen bond interactions in the binding of hISG15.

To gain a better understanding of the residues mediating specificity for Ub or ISG15, we constructed mutants targeting the palm and fingers regions of the SARS-CoV PLpro, and their catalytic activities toward various substrates were determined (Fig. 5 and Table 1). These substrates included Ub- and ISG15-AMC, which are composed of the respective substrate derivatized with the fluorescent leaving group 7-amido-4-methylcoumarin. Additionally, the small peptide Z-RLRGG representing the consensus recognition sequence for both Ub and ISG15 that is also attached to AMC was included to probe for potential changes affecting protein–protein interactions *versus* changes that impact intrinsic catalytic activity.

One of the mutants, M209A, reduces the activity toward Ub-AMC by almost twofold and increases its activity toward Z-RLRGG-AMC by nearly fivefold while retaining wild-type levels of activity for ISG15-AMC. From a structural prospective, the reduction of Ub-AMC activity is not surprising as M209A shrinks the hydrophobic patch that engages the Ile44-centered hydrophobic patch in Ub. The observed increase of the activity toward Z-RLRGG-AMC is less straightforward. M209 lacks direct interaction with the
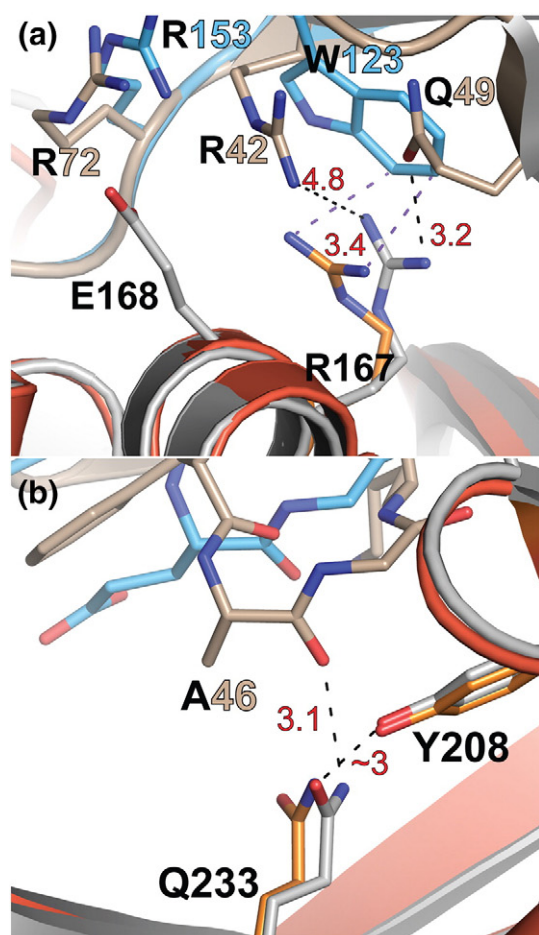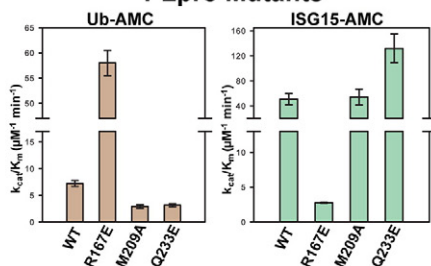
Fig. 5. (a and b) Sites within the ChISG15- and Ub-bound SARS-CoV PLpro structures corresponding to the mutations causing increased Ub-AMC activity (top) *versus* increased ISG15-AMC activity (bottom). Structures shown as cartoons, colored as in Fig. 4c. Intermolecular distances to indicate proximity for SARS-CoV PLpro–Ub are shown as black dashes with the ones for SARS-CoV PLpro–ChISG15 in purple. (c) Activity of SARS-CoV PLpro mutants toward Ub- and ISG15-AMC. Corresponding data found in Table 1.

last 5 aa of Ub or ISG15. However, its replacement by alanine could sterically open up a space that is more accommodating for the artificial Z-adduct of the peptide. The other two mutants were found to have

increased catalytic efficiencies for processing either Ub or ISG15 with a corresponding reduction in activity for the other. R167E is over 8 times more efficient than the wild-type enzyme at hydrolyzing Ub but is about 20 times less efficient at hydrolyzing ISG15 (Fig. 5c). In contrast, Q233E is nearly threefold more efficient than wild-type at hydrolyzing ISG15 and twofold less efficient at hydrolyzing Ub. In the case of Ub, the mono-Ub structure suggests that the charge flip with R167E may introduce an additional electrostatic interaction with either Arg42 or Gln49 of Ub. For the ChISG15 structure, this change occurs in close proximity to the interaction between Trp123 and Met209. Examination of the structure reveals that Arg167 may contribute to π–π interactions involving Trp123 and Arg153 of ChISG15 (Figs. 4e and 5a). Replacing the longer and positively charged arginine with the shorter glutamate removes this contribution. Additionally, this charge flip may disrupt the electrostatic interaction between Arg153 and Glu168 of the PLpro, potentially resulting in a loss of affinity for ChISG15. For Q233E, the change from a neutral polar to a charged group may create a potential electrostatic repulsion with the backbone carbonyl of Ala46 in Ub (Fig. 5b). For the ChISG15 structure, in comparison, there is not a clear direct interaction between PLpro and ISG15 that would be affected. This suggests that the impact of this mutation may stem from internal changes within the PLpro regarding the flexibility of the finger region rather than direct interactions with the substrate.

X-ray structure of SARS-CoV PLpro bound to the C-terminal domain of mISG15

In light of the differences in the nature of interactions between different species' ISG15s revealed by ITC, and the apparent plasticity that can occur between Ub and hISG15 within the SARS-CoV PLpro active site, insights into the structural sources of this phenomenon were sought. To this end, a structure of SARS-CoV PLpro with CmISG15 was determined to a resolution of 2.4 Å (Fig. 6a). The structure of the catalytic core domain of SARS-CoV PLpro is consistent with the structure of the ChISG15 SARS-CoV PLpro structure. However, a major difference in the orientation of the Ubl domain of SARS-CoV PLpro is observed when bound to CmISG15. Unlike previous SARS-CoV PLpro structures where the Ubl domains differ only slightly in its position/orientation to the catalytic domain or are unobservable because of weak electron density, suggesting potential flexibility, the Ubl in the SARS-CoV PLpro–CmISG15 structure takes a sharp, almost 90° turn in orientation when compared with previous X-ray structures (Fig. 6c). The new orientation does not appear to form contacts with the bound CmISG15, suggesting that there is no direct influence on the Ubl domain to adopt this conformation. Further analysis of the new orientation reveals a seam

Table 1. Kinetic parameters of SARS PLpro WT and mutants with different ubiquitin-based fluorescent substrates

Substrate	SARS PLpro enzymes			
Kinetic parameters	WT	R167E	M209A	Q233E
RLRGG-AMC[a] k_{cat}/K_m (μM^{-1} min^{-1})	0.141 ± 0.002	0.062 ± 0.001	0.727 ± 0.007	0.211 ± 0.002
Ub-AMC[a] k_{cat}/K_m (μM^{-1} min^{-1})	7.22 ± 0.56	58.0 ± 2.5	2.90 ± 0.32	3.14 ± 0.32
ISG15-AMC[b] k_{cat}/K_m (μM^{-1} min^{-1})	50.7 ± 9.0	2.76 ± 0.10[a]	54.3 ± 12.8	132 ± 23

[a] Best-fit slope values derived k_{app} for nonsaturating substrates and approximates k_{cat}/K_m.
[b] Steady-state values following Michaelis–Menten kinetics are reported from duplicate measurements.

made up of several electrostatic interactions between the Ubl domain and the thumb domains of the PLpro, indicating that this orientation can be stabilized (Fig. 6b).

The Ubl domain was not the only global difference between the SARS-CoV PLpro–CmISG15 and SARS-CoV PLpro–ChISG15 complexes. Surprisingly, the global orientation of CmISG15 is tilted 27° away from the fingers in SARS-CoV PLpro (Fig. 6d). Interestingly, 4 aa appear to explain the lack of CmISG15's accommodation in the same orientation to that of bound ChISG15. At position 149 in ChISG15 and 147 in CmISG15, there is an amino acid difference of a phenylalanine and an isoleucine, respectively (Fig. 6e). This change in CmISG15 eliminates the hydrophobic interaction with the finger region of SARS-CoV PLpro seen in the ChISG15-bound structure and likely aids in the tilt toward the Ubl domain. In addition, there is a change from Asn89, Thr125, and Asn151 in ChISG15 to Glu87, Ser123, and His149 in CmISG15 (Fig. 6f). These amino acid differences create a hydrogen bond network among Glu87, His149, and Ser123 in the CmISG15, which is absent in the ChISG15-bound structure. This network locks the Glu87 into an unfavorable position for CmISG15 to bind in the same manner as ChISG15. The unfavorable position ultimately results in the repulsion of CmISG15 against PLpro.

In concert with a loss of the hydrophobic interaction with the finger region and potential electrostatic repulsions that CmISG15 would incur in binding in the same orientation of ChISG15, the CmISG15 bound orientation facilitates the formation of numerous favorable interactions. Consistent with the X-ray structures of other deISGylases bound to the C-terminal domain of hISG15 [27,28], the conserved Trp121 of mISG15 is centric to the interface. However, unlike the interaction observed in the SARS-CoV PLpro–ChISG15 structure, Trp121 in the mISG15 does not insert into a hydrophobic pocket. Instead, mISG15's Trp121 and Pro128 form significantly smaller hydrophobic interaction with SARS-CoV PLpro via the proteses' extended alkyl chain of Glu168 generated by the hydrogen bond formed between it and Thr171. In contrast to the bound ChISG15 and outside the last five C terminus consensus amino acids of Ub and ISG15, this weak hydrophobic interaction between CmISG15 and the protease is the only one observed. In addition to the hydrophobic binding contributions of mISG15 Trp121, a water molecule is observed to mediate a hydrogen-bonding network between Trp121's indole nitrogen and several nearby PLpro residues (Fig. 6g and h). Including this hydrogen bond network, CmISG15 forms almost 40% more hydrogen bonds with the protease that is then observed with ChISG15. One set of these additional

Fig. 6. (a) Cartoon representation of the SARS-CoV PLpro complexed with CmISG15 (green). Secondary structure of the PLpro is designated, with helices and loops rendered in gold, and β-sheets rendered in silver. The structural domains of the PLpro are identified, consisting of the fingers (white), palm (purple), thumb (green), and Ubl (red) labeled with colored boxes. (b) Cartoon representation in wall-eyed stereo view, with transparent surfaces, of the interactions between the thumb domain (gold) and Ubl domain (gray) for the SARS-CoV PLpro–CmISG15-bound structure. Amino acids involved in interactions are represented as sticks, and hydrogen bonds are indicated by black dashes and distances (Å) labeled in red. (c) Ribbon overlay of SARS-CoV PLpro complexed with CmISG15 (gold), and SARS-CoV PLpro complexed with ChISG15 (reddish orange) demonstrating the movement of the Ubl domain. (d) Overlay of SARS-CoV PLpro (gold) complexed with CmISG15 (green) and the ChISG15 (blue) from the SARS-CoV PLpro complex based on a secondary structure alignment of the respective PLpros. The approximate degree of shift in the orientation of analogous α-helices is indicated. (e and f) Comparison between the SARS-CoV PLpro (reddish orange) complexed with ChISG15 (blue) and CmISG15 (green). Electrostatic interactions indicated with black dashes and distances (Å) labeled in red or yellow, respectively. (g and h) Interactions between SARS-CoV PLpro (gold) and CmISG15 (green) with electrostatic interactions indicated with black dashes, distances (Å) labeled in red, and hydrophobic interactions indicated by the yellow transparent surface.

electrostatic interactions are centered on SARS-CoV PLpro's Arg83 and CmISG15's Lys132. Others are also observed to form between SARS-CoV PLpro's Asn157, Gln175, and Arg167 and CmISG15's Glu130, the carbonyl of Gly126, and His149, respectively (Fig. 6g and h).

Taken overall, the interface of bound CmISG15 of 872.5 Å^2 is similar in size to that of the ChISG15's ~767 Å^2 interface, but it consists of predominately electrostatic interactions, whereas the former has a significantly greater hydrophobic component. In line with this, a greater number of water molecules, approximately 10, can be observed within the interface, further indicating the degree to which binding may be driven by more hydrophilic interactions. This characterization of the binding
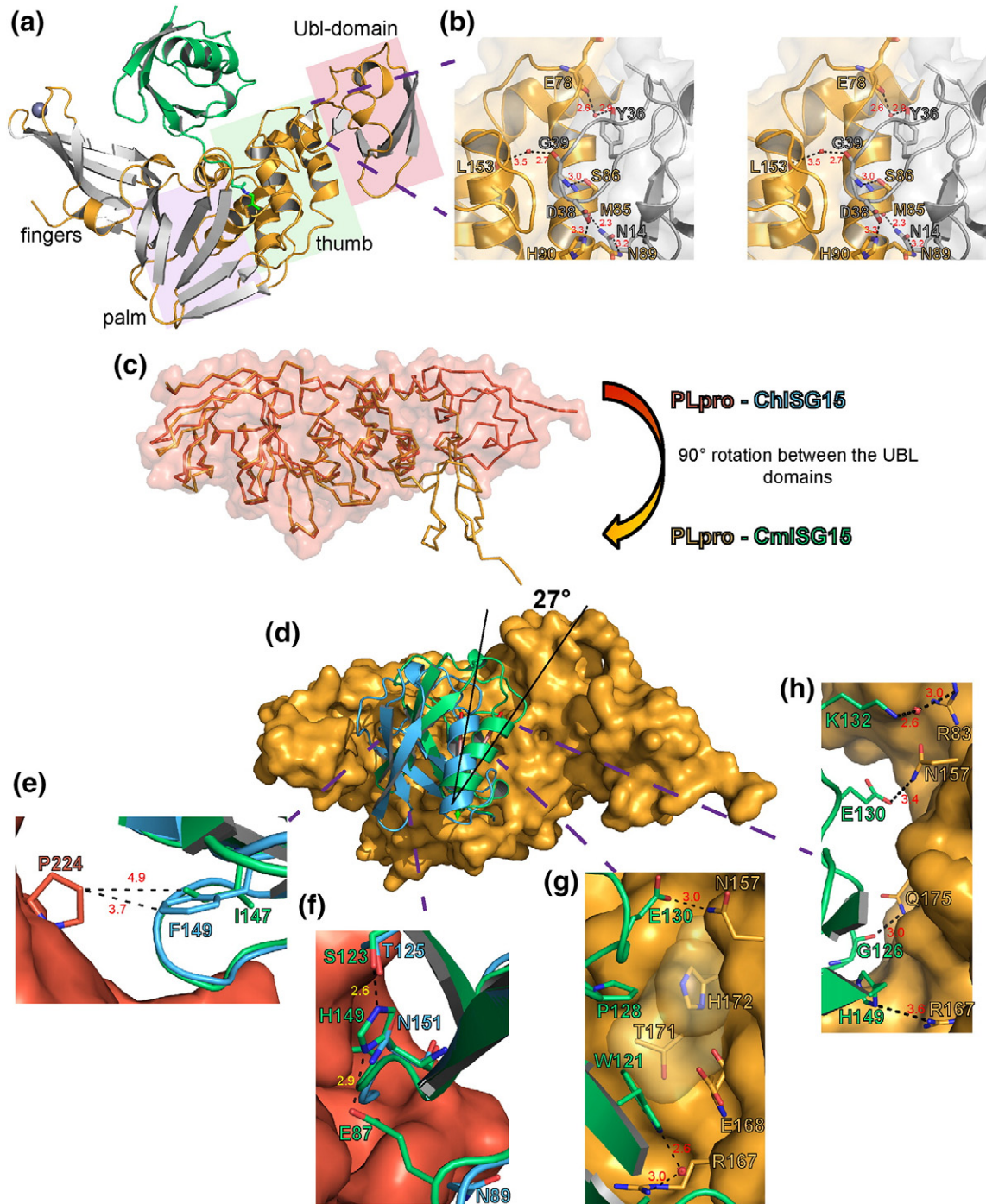

Fig. 6 (*legend on previous page*)

Table 2. Isothermal titration calorimetry

Protein	N (sites)	K_D (μM)	ΔH (kJ/mol)	ΔG (kJ/mol)	$-T\Delta S$ (kJ/mol)
SARS-CoV PLpro					
Human	0.932 ± 0.032	20.50 ± 4.48	−27.20 ± 1.90	−26.80	0.38
C-Human	1.31 ± 0.015	57.6 ± 3.21	−4.03 ± .019	−24.18	−20.17
Sheep	1	200 ± 41	−106 ± 10	−21.10	84.8
Mouse	1	196 ± 68	−92 ± 15	−21.20	70.4
C-Mouse	1	1870 ± 173	−20.71 ± 0.486	−15.56	5.10
MERS-CoV PLpro					
Human	0.785 ± 0.027	59.3 ± 12.7	−11.34 ± 0.268	−24.15	−12.80
Sheep	1	172 ± 38.5	−19.92 ± 0.420	−21.51	−1.59
Mouse	1	376 ± 52.8	−43.51 ± 0.535	−19.54	24.10

interaction is consistent with the thermodynamic properties observed for the binding of CmISG15 to SARS-CoV PLpro (Table 2). Also, when viewed in conjunction with the affinity data of mISG15 and hISG15 and their C-terminal domain counterparts, it suggests that the type of interface formed between CmISG15 and SARS-CoV PLpro is less stable than its ChISG15 counterpart and may be one of the contributing factors to the overall reduction in binding affinity observed for full-length mISG15 when compared to hISG15 via ITC.

X-ray structure of the full-length, unbound form of mISG15 and comparison with hISG15

Whereas some viral deISGylating enzymes, such as vOTUs, are thought to exclusively interact with the C terminus of ISG15, SARS PLpro has been shown to contain two Ub-binding sites that likely engage the N terminus of ISG15s [11,15]. With only the full-length hISG15 structure available, the impact of ISG15 biodiversity within the N-terminal region has been difficult to assess. To address this issue, we determined the X-ray structure of mISG15 with both domains to assess the conformational variability of mISG15 compared to hISG15. Initially, only a low-resolution (4 Å) structure could be determined. Truncation of the last non-structured 5 aa led to a structure that could be determined to a higher resolution of 3.25 Å. Using the program Define Secondary Structure of Proteins (DSSP), the secondary structure of mISG15 was determined to be comparable to hISG15. mISG15 contains nine beta sheets, two helices, but only two 3_{10} helices within the C-terminal domain; this differs from the hISG15 that contains two 3_{10} helices per domain of ISG15 (Fig. 7a) [29]. The asymmetric unit consists of 2 twisting filaments, containing 10 copies of mISG15. Upon examining the differences between the monomers within the asymmetric unit, some flexibility between N- and C-terminal domains was observed (Fig. 7b and c). This flexibility was probed by aligning the C-terminal domains of each mISG15 monomer and measuring

the angle between the point of divergence and the farthest N termini. There is a 20.2° range of motion between the N- and C-terminal domains of mISG15 (Fig. 7b). Comparable flexibility was also observed in hISG15 structures, with an 18.3° range of motion (Fig. 7c; PDB entries: 1Z2M, 3R66, 3PSE) [27,29,30].

While each individual domain of hISG15 and mISG15 is similar in the secondary structure and both show some structural variability between monomers, there is a drastic difference in the overall conformations of the tertiary structures between mISG15 and that of hISG15. This surprising difference is observed in the overall arrangement of the N- and C-terminal domains. Specifically, the twist about the C- and N-terminal domain of mISG15 in relation to hISG15 ranges from 43.0° to 66.9° (Fig. 8a). Closer investigation reveals that differences in tertiary arrangement can be attributed to several molecular interactions within the structures driven by the primary sequence differences of mISG15 compared to hISG15. Specifically, the presence of Asp79 creates a kink in the hinge region of hISG15 as a result of the carboxylate group of Asp79 forming a hydrogen bond with the hydroxyl group of Thr101 (Fig. 8b). This interaction does not occur in mISG15 since Ser77 replaces Asp79.

While amino acids in the hinge may play a part in the different conformational trajectory allowed in the region between the two domains in mISG15, the twisted feature of mISG15 may be stabilized by amino acid interactions in the core region of the protein. This core region is centered near Phe41, at the interface between the two domains. The hydrophobic interaction between the N-terminal and C-terminal domain at Leu134 and Phe41 may stabilize mISG15s' twisted arrangement (Fig. 8b). Other residues in close proximity, such as Pro39, appear to further stabilize this hydrophobic interaction in mISG15. Specifically, Pro39 in mISG15 forms hydrophobic interactions with Phe41, contributing to the stabilization of mISG15s' tertiary arrangement (Fig. 8b).
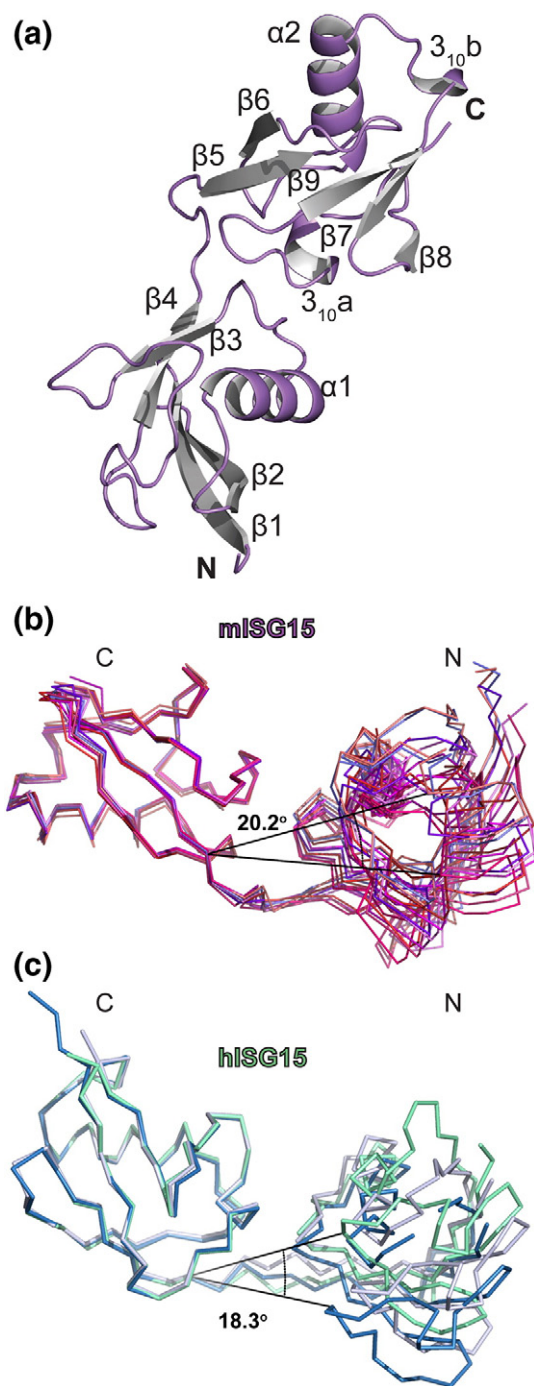
Fig. 7. (a) Secondary structure of monomer A of full-length mISG15 (purple) with β-sheets colored in silver. (b) Monomers of mISG15 were overlaid, aligning the C-terminal domains, to observe the flexibility of the monomeric units. (c) Monomers of hISG15 (green, PDB entry: 1Z2M; gray, PDB entry: 3R66; blue, PDB entry: 3PSE) were overlaid, aligning the C-terminal domains, to observe the flexibility of the monomeric units.

In addition to the presence of favorable interactions, steric clashes are also likely responsible for preventing the occurrence of a shared tertiary arrangement

between the mISG15 and hISG15 species. When the N-terminal and C-terminal domains of mISG15 are configured to the arrangement of hISG15, there are no obvious clashes that prohibit mISG15 from adopting this conformation (Fig. 8c). However, hISG15 may be incapable of adopting the mouse conformation due to the potential steric clash between His39 and Glu139 that typically forms a water-mediated interaction (Fig. 8c). Thus, the presence of the His39 residue may prevent hISG15 from configuring to the mISG15 conformation.

Beyond the effects on tertiary structure, the sequence divergence between mISG15 and hISG15 also impacts the potential binding surfaces. These differences in amino acid sequence also give rise to different electrostatic potential plots. Unlike mISG15, hISG15 contains an uninterrupted negative surface band spanning across the two domains (Fig. 8d). When the surface of mISG15 corresponding to the same area is examined, this negative band dissipates as the comparable area on mISG15 is scattered with positive and neutral areas.

Discussion

Differences in hISG15 and mISG15 structure influence recognition by PLPs

Among Ub and Ubl proteins, ISG15 is unique for more than its divergent amino acid sequence. Similar to other Ubl proteins, ISG15 has not been observed to form polymeric chains like Ub [31]. However, ISG15 is the sole family member of Ubl modifiers that is composed of two Ubl folded domains. These two domains are tethered by a polypeptide linker that would suggest that the two domains can move freely and independent of each other. However, the four structures of hISG15 alone, or bound to viral proteins, suggest the opposite (Fig. 7c) [27–30]. Akin to polymeric Ub, ISG15 appears to have relatively limited conformations between the two domains. The structure of mISG15 (Fig. 7b) furthers this assertion with one important caveat: one species' ISG15s domain configuration may not be necessarily representative of others or ISG15s in general.

In both hISG15 and mISG15, there is a hydrophobic interface mediated by a conserved phenylalanine (Phe41; see Fig. 8). The highly conserved nature of this phenylalanine and other surrounding residues suggests that ISG15s in general likely utilize hydrophobic forces to adhere the two domains together (Fig. 1b, residues involved are boxed in blue). However, as shown with mISG15, the influence of the core on the orientation of the domains can vary. In mISG15, residues forming the core solely dictate its interdomain orientation, whereas in hISG15,
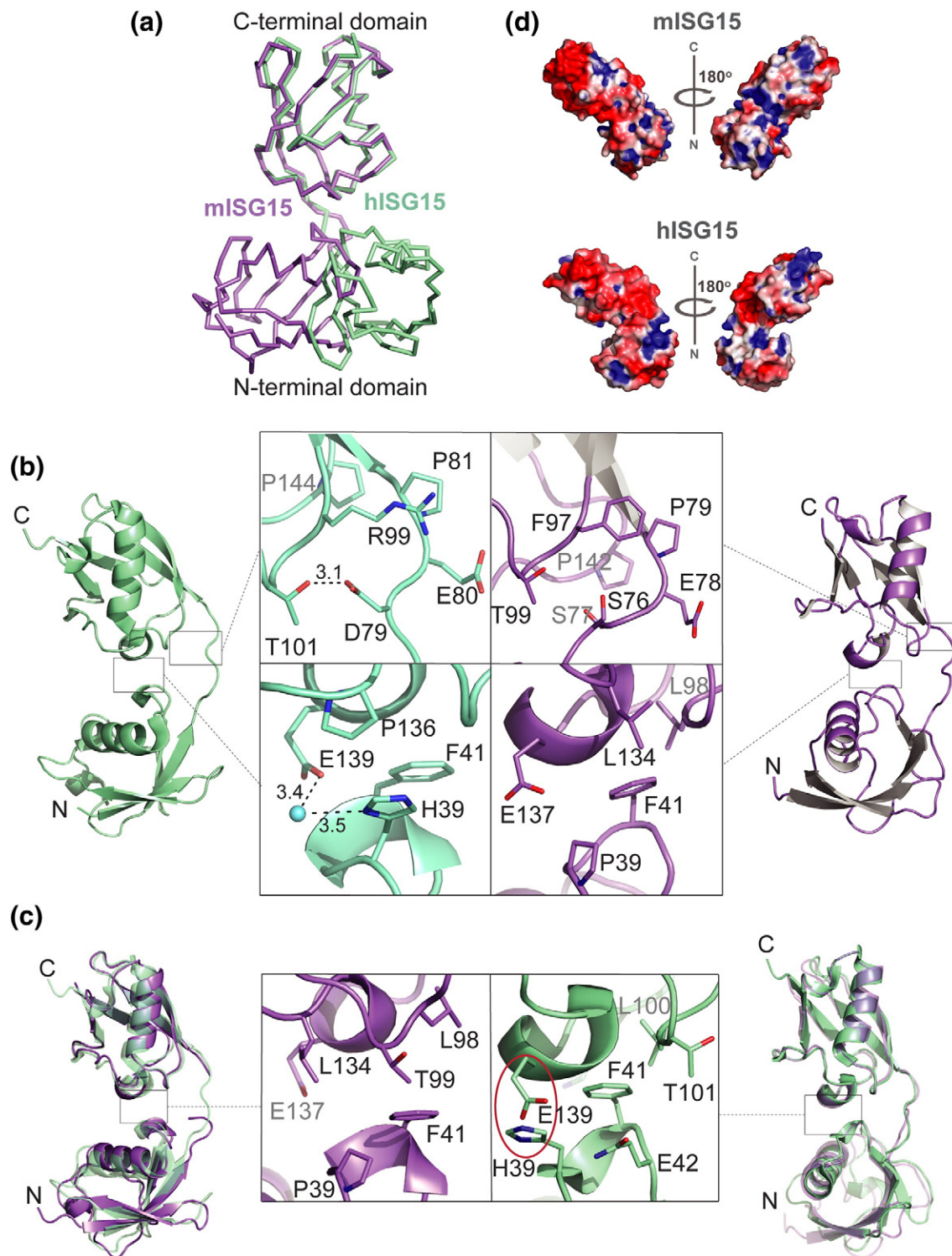
Fig. 8. (a) Overlay of mISG15 (purple) and hISG15 (green, PDB entry: 1Z2M) shown in ribbons. (b) Comparison of interactions responsible for the structural conformations of hISG15 (green) and subunit A mISG15 (purple) with dashed lines representing bond lengths in Å. (c) Interactions observed when mISG15 is forced into the hISG15 conformation (left panel) and vice versa (right panel). (d) Electrostatic surface of mISG15 and hISG15.

additional electrostatic interactions involving Glu139 and His39, and to a lesser extent Thr101 and Asp79, appear to play an additional role to favor one orientation over another (Fig. 8b and c). Intriguingly, the pairing of Glu139 and His39 is extremely unique to hISG15. Although Glu139 or another acidic residue is well conserved at that position, His39 is typically a proline. In hISG15, it appears that this favorable electrostatic interaction may promote hISG15's domain orientations. Multiple crystal structures reveal this conformation to be consistent despite differences in space groups and crystallization conditions, suggesting that the observed tertiary structure is a stable and likely preferred conformation (Fig. 7c). In addition to favoring hISG15's conformation, His39 may also act as a steric block preventing hISG15 from adopting a similar tertiary structure and conformation as that of mISG15.

The observation of a potential steric block may result in MHV PLP2 not being able to recognize hISG15, which is why no cleavage of pro-hISG15 is observed (Fig. 2). In contrast, no apparent steric hurdle is present for mISG15 in adopting a hISG15-like interdomain orientation, which is likely why SARS-CoV and MERS-CoV PLpro are able to readily recognize mISG15. The lack of a steric hurdle might suggest that there are more allowable domain arrangements of mISG15 than hISG15 in solution that allow for a broader spectrum of PLPs to recognize mISG15. The potential uniqueness of hISG15's structure may also fall in line with the inability of other viral proteins, such as influenza NS1, to effectively engage ISG15s beyond those of human and primates [30]. Moreover, the distinctiveness of hISG15 may also fit into the recent assertions that hISG15 plays a divergent immune regulation role in humans compared to other animals [32].

Viral USP-like PLPs' accommodation of Ub *versus* ISG15s

Ub interactions with proteins possessing a Ub-binding site have been observed to be reliant largely on the involvement of a hydrophobic patch composed of several residues surrounding Ile44 [15]. The absence of such a comparable patch in ISG15 and the more generally charged surface of hISG15 naturally spurred speculation on mechanisms behind how PLPs may engage ISG15s. The SARS-CoV PLpro–ChISG15 complex reveals that in PLPs, the binding interface may have evolved to recognize specific features of ISG15s from different species outside the 5-aa C-terminal sequence (Arg-Leu-Arg-Gly-Gly) they share with Ub. For hISG15, this includes not only the highly conserved Trp123 of ISG15s but also the specific interactions that are unique to hISG15. For instance, Arg87 in hISG15 is often substituted for a lysine residue that is too short to form any water-mediated

interactions with the SARS-CoV PLpro's Asp230 and Ser222. Interestingly, Phe149, which forms a second hydrophobic interaction site with the protease's Pro224, is one of the 3 aa recently implicated in species specificity among nairovirus vOTUs [23]. Residue changes between hISG15 and mISG15 at the other two positions, Asn151 and Asn89, appear to impede the accommodation of mISG15 in the active site of SARS-CoV PLpro compared to the more favorable hISG15 orientation. This appears to advocate that differences at these three ISG15 positions have a broader range of influence beyond only one class of viral proteases and could conceivable represent an evolutionary pressure that underlies a part of ISG15 sequence diversity. Also, SARS-CoV residues that interact with these residues and SARS-CoV PLpro deubiquitinating and deISGylating altering mutants, R167E, M209A, and Q233E, may offer advantageous starting points for developing SARS-CoV PLpros with directed shifts in substrate specificities.

Beyond the C-terminal domains' interaction with PLPs, the N terminus of hISG15 has been previously proposed to interact with a ridge helix spanning the conical PLP thumb domain with the Ubl domain to enhance affinity. Currently, no X-ray structures of a PLP with full-length ISG15 exist, and previous computational models utilizing existing SARS-CoV PLpro structures bound with mono-Ub have had difficulty reconciling the significant gap that occurs between hISG15's N-terminal domain and the protease when anchoring C-terminal hISG15 domain on bound Ub. The SARS-CoV PLpro–CxISG15 structures offer two synergistic explanations. First, the 6.3-Å shift of ChISG15 relative to bound Ub translates the N-terminal domain toward the ridge helix (Fig. 9a). In addition, the alternate Ubl conformation found in the SARS-CoV PLpro–CmISG15 structure reveals that such a conformation translates the ridge helix up to 14 Å toward the location of the ridge helix (Fig. 9b and c). Interestingly, comparing this model to the X-ray structure of SARS-CoV PLpro bound to K48-linked di-Ub highlights that different facets of the Ubl fold found in the N-terminal domain ISG15 are likely involved in the interaction (Fig. 9d). Specifically, in this model, a triple serine repeat, Ser20–22, and Glu27 located in hISG15's β2α3 loop and α3, respectively, point toward the protease's ridge helix, creating a surface that is available to be engaged by the bevy of charged and polar residues located on SAR-CoV PLpro's ridge helix that has been previously implicated in binding [15]. These potential electrostatic interactions may contribute to the four-times-larger enthalpy binding component observed in the interaction of full-length over the C-terminal domain of hISG15 when being accommodated by SARS-CoV PLpro. The impact of mISG15's divergent domain orientation from hISG15 is also apparent. Initial molecular modeling of the hISG15

structure onto the CmISG15-bound SARS-CoV PLpro structure with CmISG15 as an anchor reveals a steric clash with the ridge helix. This is the same for hISG15 drawn from any of its known X-ray structures. However, the divergent interdomain orientation found in full-length mISG15 structure determined
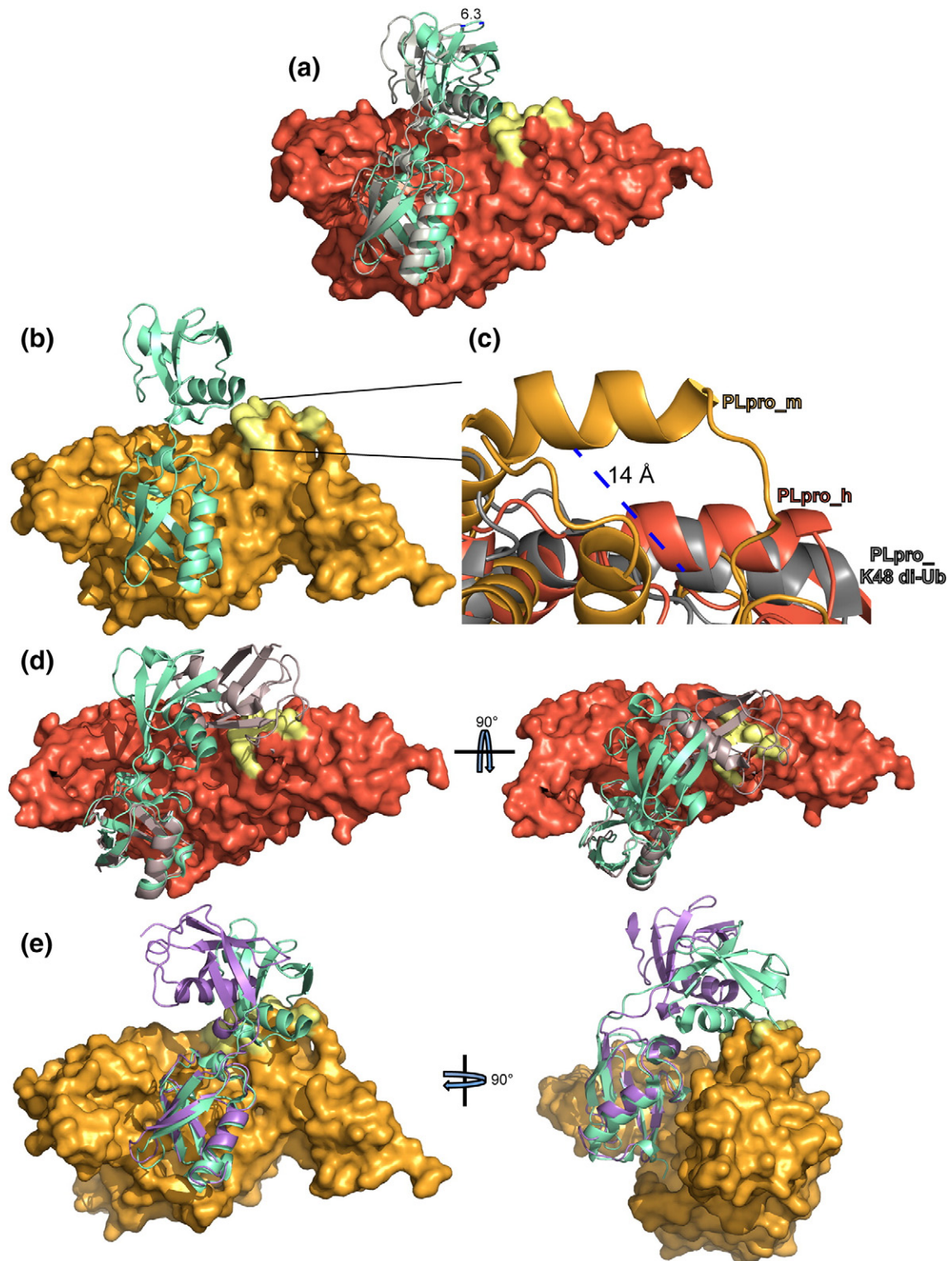

Fig. 9 (*legend on next page*)

here allows for the mISG15's N-terminal domain to fit unobstructed (Fig. 9e). The significant domain–domain orientation differences between hISG15 and mISG15 result in a different facet of mISG15 facing the protease. Specifically, mISG15's α1β3 loop comprises the surface oriented toward the ridge helix presenting a polar interface that ITC suggests may be involved in forming additional electrostatic interactions beyond those of the C-terminal domain. However, when comparing the ITC data for full-length and its CmISG15 counterpart, these additional interactions might potentially come at an ethalpic cost. This may suggest that different ISG15 N-terminal domains may engage the protease's ridge helix to differing degrees and thermodynamic characteristics. The need for PLPs to accommodate not only surface differences between species ISG15s but also divergent interdomain orientations highlights the difficulties for a CoV PLP to be active to all species ISG15s. This could also be perceived as a possible benefit to ISG15's unique tandem Ubl arrangement. Also, the improved structural perspective on how the N terminus of ISG15s from different species may engage CoV PLPs provides a clearer path toward utilizing this region to influence the deISGylating activities of CoV PLPs. As a result, combining this information along with the alterations possible in the C-terminal domain, we can envision fresh tools to address the role of deubiquitination and deISGylation through the use of reverse genetics systems.

Possible evolution of CoV PLP recognition of species variances in ISG15s

Overall, the X-ray structural, enzymatic, and biophysical data point to CoV PLP deISGylase activities being sensitive to species-specific amino acid differences within ISG15. Intriguingly, SARS-CoV and MERS-CoV PLpros, whose viruses replicate in a wide range of hosts, recognize and cleave proISG15 from almost all of the species tested. In contrast, the mouse-specific MHV PLP2 is limited predominantly to the mouse substrate. This wider range of specificities appears substantially larger than that found recently in nairovirus vOTUs. This may imply that with the greater binding interface provided by the palm, fingers, and thumb domains of the USP fold, CoV PLPs can either engage a wider array of ISG15s than that of vOTUs or be highly selective for just one or two ISG15s as in the case of MHV.

Intriguingly, in all of the PLPs examined, their potential ability to engage different species ISG15s is not fully restricted to only those from species their parent viruses infect. Understandably, this could be a by-product in the evolutionary process of a specific viral protease seeking to optimize toward a certain species ISG15 and inadvertently picking up enzymatic activity toward another ISG15; or, in an environment where a virus only has to optimize its replication in one species, there is less selective pressure and hence a greater chance of losing the ability of recognizing ISG15s from other species. Alternatively, some of these types of off-species PLP activities could be indicative of evolutionary memory for ISG15s. In essence, this could give a possible view into the zoonotic evolutionary history or potential future zoonotic drift for a certain virus. Naturally, a wider sampling of CoV PLPs' affinities for certain species ISG15s, knowledge of what species their parent viruses infect, and a multitude of reverse genetics experiments will be necessary to discern which of the above scenarios take place in the evolution of virus recognition of host ISG15s.

Materials and Methods

Construct, expression, and purification of PLPs for the ISG15 protease activity assay and ITC

MHV PLP2 was expressed and purified as previously described [10,24]. SARS-CoV PLpro in expression vector pET21a and MERS-CoV PLpro in pET15b were transformed into *Escherichia coli* BL21(DE3) competent cells (New England Biolabs)

Fig. 9. (a) SARS-CoV PLpro (reddish orange) from the ChISG15-bound structure with full-length human (green, PDB entry: 1Z2M) overlaid with full-length human based off of a secondary alignment using Ub (light gray, PDB entry: 4MM3). The distance between the two overlaid, full-length human structures is measured in Å and is indicated by a blue dashed line. For all figures, the highlighted yellow portion demonstrates the secondary binding site ridgeline. (b) SARS-CoV PLpro (gold) from the CmISG15-bound structure with full-length human (green, PDB entry: 1Z2M) based off of a secondary structure alignment using ChISG15. (c) Closeup overlay of the secondary binding site helix from SARS-CoV PLpro (gold) from the CmISG15-bound structure, SARS-CoV PLpro (reddish orange) from the ChISG15-bound structure, and SARS-CoV PLpro (dark gray, PDB entry: 5E6J) from the K48 di-Ub-bound structure. The distance between the helix from SARS-CoV PLpro (gold) from the CmISG15-bound structure and the helix from SARS-CoV PLpro (reddish orange) from the ChISG15-bound structure is measured in Å and is indicated by a blue dashed line. (d) SARS-CoV PLpro (reddish orange) from the ChISG15-bound structure with full-length human (green, PDB entry: 1Z2M) overlayed with K48 di-Ub (dark brown, PDB entry: 5E6J) both based off of a secondary alignment using ChISG15. (e) SARS-CoV PLpro (gold) from the CmISG15-bound structure with full-length mouse overlaid with full-length human (green, PDB entry: 1Z2M) both based off a secondary structure alignment using CmISG15.

by heat shock. Cells were grown at 37 °C in LB broth supplemented with 100 µg/mL of ampicillin to OD_{600} of 0.6–0.8, and expression was induced with 0.8 mM IPTG at 25 °C overnight for SARS-CoV PLpro and 1 mM IPTG at 18 °C overnight for MERS-CoV PLpro. Cells were collected by centrifugation at 6000g for 10 min and stored at −80 °C. Cells were lysed in Buffer A [20 mM Tris (pH 7.5 for SARS-CoV PLpro and pH 7.0 for MERS-CoV PLpro), 500 mM NaCl, and 10 mM β-mercaptoethanol (BME)] supplemented with lysozyme for 30 min at 4 °C, followed by sonication on ice at 50% power with a 50% duty cycle for a total of 6 min. Insoluble protein was removed by centrifugation at 70,600g for 30 min and the supernatant filtered through a 0.8-µm filter. The clarified supernatant was flowed over high density nickel agarose beads (Gold Biotechnology, Olivette, MO) pre-equilibrated with Buffer A. The column was washed with 10 column volumes of Buffer A supplemented with 30 mM imidazole, and the protein was eluted with 10 column volumes of Buffer A supplemented with 300 mM imidazole. The PLpro was further purified by size-exclusion chromatography using a Superdex 200 column (GE Healthcare, Pittsburgh, PA) pre-equilibrated with 100 mM NaCl, 5 mM Hepes (pH 7.5 for SARS-CoV PLpro and pH 7.0 for MERS-CoV PLpro), and 2 mM DTT.

Purification of SARS-CoV PLpro for complexation and crystallization

Purification of SARS-CoV PLpro in expression vector pET11a for complexing with ChISG15 and CmISG15 was adapted from the previously described method [7]. The cells were chemically lysed by resuspending them in 150 mL of Buffer B [20 mM Tris (pH 7.5) and 10 mM BME] and lysozyme and were incubated at 4 °C for 30 min. The suspension was sonicated on ice at 50% power with a 50% duty cycle for a total of 6 min and centrifuged for 30 min at 40,900g. The cell lysate was filtered and subjected to a 40% ammonium sulfate fractionation then centrifuged again for 30 min at 40,900g. The resulting pellet was resuspended in 250 mL of 1 M ammonium sulfate, 20 mM Tris (pH 7.5), and 10 mM BME and incubated at room temperature for 1 h. The suspension was filtered and loaded onto a 50-mL Phenyl-Sepharose CL-4B column (GE Healthcare, Pittsburgh, PA) equilibrated with 1.5 M ammonium sulfate, 20 mM Tris (pH 7.5), and 10 mM BME. The protein was eluted using a 10-column-volume gradient to 100% Buffer B and washed with 2 additional column volumes of 100% Buffer B. The fractions were pooled together and then diluted fivefold with Buffer B. The protein was loaded onto a MonoQ 10/100 column (GE Healthcare, Pittsburgh, PA) equilibrated with Buffer B. The protein was eluted using a 10-column-volume gradient to 100% of a buffer composed of 0.5 M NaCl, 20 mM Tris (pH 7.5),

and 10 mM BME with the initial flow-through off the column collected. The flow-through was concentrated and put into dialysis in a 50 mM NaCl, 20 mM Tris (pH 7.5), and 10 mM BME buffer at 4 °C overnight.

Construct, expression, and purification of proISG15s and mature ISG15s

ISG15s from human (*H. sapiens*; Accession: AAH09507.1), mouse (*Mus musculus*; Accession: AAB02697.1), northern tree shrew (*Tupaia belangeri*; Accession: AFH66859.1), sheep (*Ovis aries;* Accession: AF152103.1), dromedary camel (*Camelus dromedarius*; Accession: XP_010997700.1), vesper bat (*Myotis davidii*; Accession: ELK23605.1), and jackknife fish (*Oplegnathus fasciatus*; Accession: BAJ16365.1) in both pro and mature forms were prepared as described elsewhere [23].

ISG15 protease activity assay

Activity assays of SARS-CoV PLpro, MERS-CoV PLpro, and MHV PLP2 with purified northern tree shrew proISG15 (pro-nsISG15), sheep proISG15 (pro-shISG15), fish proISG15 (pro-fISG15), mouse proISG15 (pro-mISG15), camel proISG15 (pro-cISG15), bat proISG15 (pro-bISG15), and human proISG15 (pro-hISG15) were adapted from the previously described methods [23].

ITC of ISG15 with PLpros from MERS-CoV and SARS-CoV

ITC was performed using a Microcal PEAQ-ITC (Malvern, Worcestershire, UK). There were 19 injections of 2 µL each at 25 °C with a reference power of 6 µcal/s. The mature forms of ISG15s along with PLpros from MERS-CoV and SARS-CoV were dialyzed at 4 °C in 50 mM Hepes (pH 7.4), 200 mM NaCl, and 1 mM DTT. All experiments were run in duplicate. For direct binding experiments, 227 µM and 276 µM of SARS-CoV and MERS-CoV PLpro, respectively, were placed in the cell with 2.3–2.6 mM of mature hISG15 in the syringe. For direct binding experiments of SARS-CoV with ChISG15, 303 µM was placed in the cell with 3.4 mM in the syringe, and for SARS-CoV with CmISG15, 393 µM was placed in the cell with 3.8 mM in the syringe. For competitive experiments related to SARS-CoV PLpro, mixtures containing 100 µM of protease with 50 µM of either sheep ISG15 (shISG15) or mISG15 were placed in the cell with 1 mM of mature hISG15 in the syringe. For competitive experiments related to MERS-CoV PLpro, mixtures containing 220 µM and 270 µM of protease with 110 µM and 170 µM of shISG15 and mISG15, respectively, were placed in the cell. The syringe contained 2.3 mM and 2.7 mM of mature hISG15 in the syringe for shISG15 and mISG15

assays, respectively. The data were processed using Microcal PEAQ-ITC Analysis Software.

Functional studies of SARS-CoV PLpro mutants

The SARS-CoV pET-15b-PLpro mutants (residues 1541–1855 of the SARS-CoV viral polyprotein) were generated using site-directed mutagenesis and the QuickChange® approach (Agilent). Expression and purification for the wild type and each mutant of the SARS-CoV PLpro were performed as previously described [33].

The steady-state kinetic parameters of SARS-CoV PLpro wild-type and mutants were determined for three different Ub-based fluorescent substrates, utilizing 7-amino-4-methylcoumarin (AMC), commonly used to assess the protease, deubiquitinating, and deISGylating activity of PLPs, including a small peptide substrate, Z-RLRGG-AMC (Bachem), Ub-AMC (LifeSensors, Inc.), and ISG15-AMC (Boston Biochem/R&D Systems). Kinetic assays with Ub-AMC and ISG15-AMC were performed on the same day and side-by-side in the same assay plate to directly compare the enzymatic activity of SARS-CoV PLpro to that of each of the mutants. The steady-state kinetic studies were also repeated for the wild type and mutants approximately 5 months apart, and the resulting duplicate data were combined for analysis. Kinetic assays with the peptide substrate were also performed in triplicate. For all experiments, the assay conditions (i.e., buffering conditions and assay volume, etc.) were set up as previously described [24]. The exception was that the stock substrates purchased from the vendors had different lot numbers. The steady-state kinetic data obtained from separate experiments performed on different days and with different substrate lot numbers helped ensure that the trends in the resulting kinetic parameters were reproducible.

The enzymatic activity of PLpro-mediated hydrolysis of the fluorophore AMC group was determined using a BioTEK Synergy H1 multimode microplate reader at 25 °C with an excitation wavelength of 360 nm (bandwidth = 40 nm) and an emission wavelength of 460 nm (bandwidth = 40 nm). The change in the relative fluorescence as a function of time (RFU/min) was monitored over a sufficient time period to allow the determination of the enzymatic rate in the steady-state region. For the ISG15-AMC assay, the substrate concentrations were varied from 0.2 μM up to 19.2 μM. The reactions were initiated by the addition of enzyme with the final enzyme concentrations as follows: 0.48 nM WT, 0.23 nM Q233E, 0.23 nM M209A, or 7.3 nM R167E. For the Ub-AMC assay, substrate concentrations were varied from 0.5 μM to 17.6 μM. The final enzyme concentrations were 3.7 nM WT, 7.3 nM Q233E, 7.3 nM M209A, or 0.23 nM R167E. For the Z-RLRGG-AMC assay, the concentrations of sub-

strate were varied from 0.8 μM to 50 μM, and the final concentration of the wild-type enzyme was 0.14 μM. To capture the initial rate of peptide hydrolysis for the M209A mutant, we used a lower enzyme concentration of 25 nM. As is typical for SARS-CoV PLpro, the enzyme could not be saturated with the Ub-AMC and Z-RLRGG-AMC substrates. As such, the kinetic response of the enzyme to these substrates was linear, and thus, the data were fit to a line to approximate the catalytic efficiency (k_{cat}/K_m) for each enzyme. For the ISG15-AMC assays, the data were fit to the Michaelis–Menten equation to determine the associated kinetic parameters (k_{cat}, K_m, and k_{cat}/K_m) for each enzyme [24]. Saturation was not attained with the R167E mutant enzyme for ISG15-AMC, and therefore, these kinetic data were also fit to a line to determine the apparent k_{cat}/K_m. The errors associated with each kinetic parameter were obtained from the best-fit line or curves for each mutant. All data, from separate experiments, were included in the fits to arrive at the final errors (Table 1).

SARS-CoV PLpro–CmISG15 and SARS-CoV PLpro–ChISG15 complex formation

Expression of CmISG15 or ChISG15 occurred using a vector pTYB2 and was purified as previously described to form a propargylamine-derivatized thioester product (CmISG15-PA, ChISG15-PA) [23]. Briefly, to obtain complex, we added directly purified protease to the mixture in equimolar ratios and incubated it for 2–4 h at room temperature and left it 4 °C overnight. To further purify the complex, we used anion exchange chromatography, eluting from a MonoQ 10/100 column using a linear gradient from 0 to 1 M NaCl (SARS-CoV PLpro–CmISG15) or 250 mM NaCl (SARS-CoV PLpro–ChISG15) with 50 mM Tris (pH 8.0 for SARS-CoV PLpro–CmISG15 and pH 9.0 for SARS-CoV PLpro–ChISG15), followed by size-exclusion chromatography on a Superdex 75 column (GE Healthcare, Pittsburgh, PA) pre-equilibrated with 100 mM NaCl, 5 mM Hepes (pH 7.5), and 2 mM DTT. For SARS-CoV PLpro–ChISG15, an additional purification step prior to anion exchange chromatography was used to eliminate residual ChISG15 by size-exclusion chromatography using a Superdex 200 column (GE Healthcare, Pittsburgh, PA) pre-equilibrated with 100 mM NaCl, 50 mM Tris (pH 7.5), and 2 mM DTT.

Crystallization of SARS-CoV PLpro–CmISG15, SARS-CoV PLpro–ChISG15, and mISG15

Purified SARS-CoV PLpro–CmISG15, SARS-CoV PLpro–ChISG15, and mISG15 were screened against a series of Qiagen NeXtal suites by hanging drop using a TTP Labtech Mosquito (TTP Labtech, Herfordshire, UK) at 8.8 mg/ml, 8.88 mg/ml, and

16 mg/ml, respectively. For SARS-CoV PLpro–CmISG15, the initial screen yielded the best crystals in a solution containing 65% (vol/vol) MPD and 0.1 M Tris (pH 8.0). These crystals were optimized using the Additive HT Screen from Hampton Research. The final SARS-CoV PLpro–CmISG15 crystals were obtained through vapor diffusion using a 500-μL reservoir with 4-μL hanging drops mixed (1:1) with protein solution and reservoir solution, which also contained 0.25 μl of 30% (wt/vol) trimethylamine *N*-oxide dihydrate. For SARS-CoV PLpro–ChISG15, the initial screen yielded the best crystals in a solution containing 0.2 M lithium sulfate, 0.1 M bis-Tris (pH 6.5), and 25% (wt/vol) polyethylene glycol (PEG) 3350. The initial crystal conditions for SARS-CoV PLpro–ChISG15 crystals were optimized along salt and PEG3350 gradients and by using the Additive Screen from Hampton Research. The final SARS-CoV PLpro–ChISG15 crystals were obtained through vapor diffusion using a 500-μL reservoir with 4-μL hanging drops mixed (1:1) with protein solution (6.99 mg/mL) and reservoir solution [0.1 M lithium sulfate, 0.1 M bis-Tris, (pH 6.5), and 22% PEG3350], which also contained 0.25 μl of 30% (vol/vol) glycerol. For mISG15, the initial screen yielded the best crystals in a solution containing 0.2 M ammonium sulfate, 0.1 M trisodium citrate (pH 5.6), and 15% (wt/vol) PEG4000. This condition was further optimized along buffer, pH, and PEG4000 gradients in addition to using the Additive Screen from Hampton Research. In conjunction with using these optimization methods, the mISG15 was shorted by 5 aa. The final crystals of the 5-aa-shortened mISG15 were obtained through vapor diffusion using a 500-μL reservoir with 4-μL hanging drops mixed (1:1) with protein solution (6.9 mg/mL) and reservoir solution [0.2 M ammonium sulfate, 0.1 M sodium acetate (pH 4.6), 12% PEG4000, and 0.2 M sodium malonate].

Crystals of SARS-CoV PLpro–CmISG15, SARS-CoV PLpro–ChISG15, and mISG15 were collected and flash frozen in liquid N_2. Cryogenic solutions for SARS-CoV PLpro–CmISG15 and SARS-CoV PLpro–ChISG15 constituted their respective mother liquors. For mISG15 crystals, they were passed from a 5% to a 12% solution (1:1:1) of glycerol, dimethyl sulphoxide, and PEG known as EDG [34]. Data sets were collected at the Advanced Photon Source (Argonne National Labs, Argonne, IL). A data set for SARS-CoV PLpro–CmISG15 was collected at the LS-CAT beamline 21G at a wavelength of 0.9786 Å using a MAR300 detector, whereas data sets for SARS-CoV PLpro–ChISG15 and mISG15 were collected at the SER-CAT beamlines 22ID and 22BM at 1 Å using MAR300hs detectors. All data sets were collected at 100 K.

Table 3. Data collection and refinement statistics

	SARS-CoV PLpro-ChISG15 (PDB entry: 5TL6)[*]	SARS-CoV PLpro-CmISG15 (PDB entry: 5TL7)[*]	mISG15 (PDB entry: 5TLA)[*]
Data collection			
Space group	$P2_12_12_1$	$P2_12_12_1$	$P2$
Cell dimensions			
a, *b*, *c* (Å)	46.9, 87.0, 221.5	76.0, 98.2, 106.6	85.8, 60.2, 172.7
α, β, γ (°)	90, 90, 90	90, 90, 90	90, 93.1, 90
Resolution (Å)	50.00–2.62 (2.67–2.62)[†]	50.00–2.44 (2.53–2.44)[†]	50.00–3.25 (3.31–3.25)[†]
R_{sym} or R_{merge}	11.1 (58.3)	9.9 (74.2)	5.2 (37.5)
$I/\sigma I$	12.7 (2.07)	18.0 (2.71)	17.4 (2.27)
Completeness (%)	98.4 (96.0)	99.1 (99.8)	98.4 (88.0)
Redundancy	5.0 (3.9)	2.4 (2.1)	2.4 (2.1)
Refinement			
Resolution (Å)	38.67–2.62 (2.71–2.62)	32.20–2.44 (2.53–2.44)	42.18–3.25 (3.36–3.25)
No. of reflections	27,644	29,886	27,929
R_{work} (%)/ R_{free} (%)	19.1/25.0	18.7/25.3	25.6/30.9
No. of atoms			
Protein	6177	6218	11,491
Ligand/ion	15	10	0
Water	133	231	0
B-factors			
Protein	49.27	61.13	86.7
Ligand/ion	59.94	57.02	0
Water	41.95	58.23	0
R.m.s.d.			
Bond lengths (Å)	0.004	0.008	0.002
Bond angles (°)	0.54	1.1	0.57

[*] Data sets collected from a single crystal for each structure.
[†] Values in parentheses are for highest-resolution shell.

Data processing and structure solutions

Data sets were indexed, integrated, and scaled using HKL-2000 [35]. All the structures were solved by molecular replacement using Phaser [36]. Subsequently, each structure was rebuilt initially using Autobuild [37] followed by successive rounds of manual model building and refinement using Coot [38] and Phenix [39]. The initial solution for the SARS-CoV PLpro–CmISG15 complex was achieved by using the catalytic core of a previous SARS-CoV PLpro structure (PDB entry: 3E9S). Density from the last 10 aa of the CmISG15 molecule served as an anchor for the initial global placement of the CmISG15 from a Erve nairovirus vOTU-CmISG15 complex (PDB entry: 5JZE). This partial model was then used as a search model along with the Ubl SARS-CoV PLpro domain from PDB entry: 4MM3 to obtain a complete global model using Phaser [36]. For the SARS-CoV PLpro–ChISG15 complex, an initial molecular replacement solution was obtained by using the core and other elements from the SARS-CoV PLpro–CmISG15 as a search model. A partial molecular replacement solution using Phaser [36] for mISG15 was obtained by searching with the CmISG15 from the Erve nairovirus vOTU–CmISG15 complex structure (PDB entry: 5JZE). This partial model was used in a sequential Phaser [36] run using a mISG15 N-terminal domain homology model based on the previously solved hISG15 structure (PDB entry: 1Z2M). All structures were validated using Molprobity [40] and have good Ramachandran statistics: SARS-CoV PLpro–CmISG15 (96% favored and 4% allowed), SARS-CoV PLpro–ChISG15 (96% favored and 4% allowed), and mISG15 (99.08% favored and 0.92% allowed). All structures have been deposited in the Protein Data Bank. Codes can be found on Table 3.

Electropotential plots

Figure renderings involving electropotential plots were performed using the PDB2PQR server and the surface generated using the adaptive Poisson–Boltzmann solver [41].

Accession numbers

All structures have been deposited in the Protein Data Bank (PDB entry: **5TL7** for SARS-CoV PLpro–CmISG15, **5TL6** for SARS-CoV PLpro–ChISG15, and **5TLA** for mISG15). Source sequences for ISG15s were GenBank numbers **AAH09507.1** for *H. sapiens*, **AAB02697.1** for *Mus musculus*, **AFH66859.1** for *Tupaia belangeri*, **ELK23605.1** for *Myotis davidii*, and **BAJ16365.1** for *Oplegnathus fasciatus*, and NCBI Reference Sequence **XP_010997700.1** for *Camelus dromedarius*. Source sequences for PLPs were GenBank numbers **AFS88944.1** for MERS CoV PLpro, **AKP80587.1** for PEDV PLP2, and **AHM88399.1** for PDCoV PLpro, and UniProtKB/Swiss-Prot numbers **P0C6U8** for SARS CoV PLpro and **P0C6V0** for MHV PLP2.

†C.M.D. and J.V.D. contributed equally to this work.

Abbreviations used:
CoV, Coronavirus; SARS-CoV, severe acute respiratory syndrome CoV; MERS-CoV, Middle East respiratory syndrome CoV; PLP, Papain-like protease (for viruses that have more than one PLpro); PLpro, Papain-like protease; MHV, mouse hepatitis virus; Ub, ubiquitin; USP, Ub-specific protease; DUB, deubiquitinating enzyme; Ubl, Ub-like; ISG15, interferon-stimulated gene product 15; IFN, type-I interferon; mISG15, mouse ISG15; vOTUs, viral ovarian tumor domain proteases; hISG15, human ISG15; ITC, isothermal titration calorimetry; CmISG15, C-terminal domain of ISG15 from mouse; ChISG15, C-terminal domain of ISG15 from human; DSSP, Define Secondary Structure of Proteins; BME, β-mercaptoethanol; AMC, 7-amino-4-methylcoumarin; PEG, polyethylene glycol.

References

[1] S. Perlman, J. Netland, Coronaviruses post-SARS: update on replication and pathogenesis, Nat Rev Microbiol 7 (2009) 439–450.

[2] R. Hilgenfeld, M. Peiris, From SARS to MERS: 10 years of research on highly pathogenic human coronaviruses, Antivir. Res. 100 (2013) 286–295.

[3] WHO. (2015). Middle East respiratory syndrome coronavirus (MERS-CoV) - Saudi Arabia. World Health Organization.

[4] Korea Centers for Disease, C. & Prevention, Middle East respiratory syndrome coronavirus outbreak in the Republic of Korea, 2015, Osong Public Health and Research Perspectives 6 (2015) 269–278.

[5] WHO. (2016). Middle East respiratory syndrome coronavirus (MERS-CoV) - Saudi Arabia. World Health Organization.

[6] V. Thiel, K.A. Ivanov, Á. Putics, T. Hertzig, B. Schelle, S. Bayer, B. Weißbrich, E.J. Snijder, H. Rabenau, H.W. Doerr, A.E. Gorbalenya, J. Ziebuhr, Mechanisms and enzymes involved in SARS coronavirus genome expression, J. Gen. Virol. 84 (2003) 2305–2315.

[7] N. Barretto, D. Jukneliene, K. Ratia, Z. Chen, A.D. Mesecar, S.C. Baker, The papain-like protease of severe acute respiratory syndrome coronavirus has deubiquitinating activity, J. Virol. 79 (2005) 15,189–15,198.

[8] K. Ratia, K.S. Saikatendu, B.D. Santarsiero, N. Barretto, S.C. Baker, R.C. Stevens, A.D. Mesecar, Severe acute respiratory syndrome coronavirus papain-like protease: structure of a viral deubiquitinating enzyme, Proc. Natl. Acad. Sci. 103 (2006) 5717–5722.

[9] B.H. Harcourt, D. Jukneliene, A. Kanjanahaluethai, J. Bechill, K.M. Severson, C.M. Smith, P.A. Rota, S.C. Baker, Identification of severe acute respiratory syndrome coronavirus replicase products and characterization of papain-like protease activity, J. Virol. 78 (2004) 13,600–13,612.

[10] A.M. Mielech, X. Deng, Y. Chen, E. Kindler, D.L. Wheeler, A.D. Mesecar, V. Thiel, S. Perlman, S.C. Baker, Murine coronavirus ubiquitin-like domain is important for papain-like protease stability and viral pathogenesis, J. Virol. 89 (2015) 4907–4917.

[11] H.A. Lindner, V. Lytvyn, H. Qi, P. Lachance, E. Ziomek, R. Ménard, Selectivity in ISG15 and ubiquitin recognition by the SARS coronavirus papain-like protease, Arch. Biochem. Biophys. 466 (2007) 8–14.

[12] S.G. Devaraj, N. Wang, Z. Chen, Z. Chen, M. Tseng, N. Barretto, R. Lin, C.J. Peters, C.-T.K. Tseng, S.C. Baker, K. Li, Regulation of IRF-3-dependent innate immunity by the papain-like protease domain of the severe acute respiratory syndrome coronavirus, J. Biol. Chem. 282 (2007) 32,208–32,221.

[13] M. Frieman, K. Ratia, R.E. Johnston, A.D. Mesecar, R.S. Baric, Severe acute respiratory syndrome coronavirus papain-like protease ubiquitin-like domain and catalytic domain regulate antagonism of IRF3 and NF-kappaB signaling, J. Virol. 83 (2009) 6689–6705.

[14] B.A. Bailey-Elkin, R.C. Knaap, G.G. Johnson, T.J. Dalebout, D.K. Ninaber, P.B. van Kasteren, P.J. Bredenbeek, E.J. Snijder, M. Kikkert, B.L. Mark, Crystal structure of the Middle East respiratory syndrome coronavirus (MERS-CoV) papain-like protease bound to ubiquitin facilitates targeted disruption of deubiquitinating activity to demonstrate its role in innate immune suppression, J. Biol. Chem. 289 (2014) 34,667–34,682.

[15] K. Ratia, A. Kilianski, Y.M. Baez-Santos, S.C. Baker, A. Mesecar, Structural basis for the ubiquitin-linkage specificity and deISGylating activity of SARS-CoV papain-like protease, PLoS Pathog. 10 (2014) e1004113.

[16] M. Békés, Gerbrand J. van der Heden van Noort, R. Ekkebus, H. Ovaa, Tony T. Huang, Christopher D. Lima, Recognition of Lys48-linked di-ubiquitin and deubiquitinating activities of the SARS coronavirus papain-like protease, Mol. Cell 62 (2016) 572–585.

[17] A.M. Zaki, S. van Boheemen, T.M. Bestebroer, A.D.M.E. Osterhaus, R.A.M. Fouchier, Isolation of a novel coronavirus from a man with pneumonia in Saudi Arabia, N. Engl. J. Med. 367 (2012) 1814–1820.

[18] T. Tsoleridis, O. Onianwa, E. Horncastle, E. Dayman, M. Zhu, T. Danjittrong, M. Wachtl, J.M. Behnke, S. Chapman, V. Strong, P. Dobbs, J.K. Ball, R.E. Tarlinton, C.P. McClure, Discovery of novel alphacoronaviruses in European rodents and shrews, Viruses 8 (2016) 84.

[19] S.R. Compton, C.B. Stephensen, S.W. Snyder, D.G. Weismiller, K.V. Holmes, Coronavirus species specificity: murine coronavirus binds to a mouse-specific epitope on its carcinoembryonic antigen-related receptor glycoprotein, J. Virol. 66 (1992) 7420–7428.

[20] H. Sridharan, C. Zhao, R.M. Krug, Species specificity of the NS1 protein of influenza B virus: NS1 binds only human and non-human primate ubiquitin-like ISG15 proteins, J. Biol. Chem. 285 (2010) 7852–7856.

[21] C. Lai, J.J. Struckhoff, J. Schneider, L. Martinez-Sobrido, T. Wolff, A. Garcia-Sastre, D.E. Zhang, D.J. Lenschow, Mice lacking the ISG15 E1 enzyme UbE1L demonstrate increased susceptibility to both mouse-adapted and non-mouse-adapted influenza B virus infection, J. Virol. 83 (2009) 1147–1151.

[22] G.A. Versteeg, A. García-Sastre, Viral tricks to grid-lock the type I interferon system, Curr. Opin. Microbiol. 13 (2010) 508–516.

[23] M.K. Deaton, J.V. Dzimianski, C.M. Daczkowski, G.K. Whitney, N.J. Mank, M.M. Parham, E. Bergeron, S.D. Pegan, Biochemical and structural insights into the preference of nairoviral deISGylases for interferon-stimulated gene product 15 originating from certain species, J. Virol. 90 (2016) 8314–8327.

[24] Y.M. Baez-Santos, A.M. Mielech, X. Deng, S. Baker, A.D. Mesecar, Catalytic function and substrate specificity of the papain-like protease domain of nsp3 from the Middle East respiratory syndrome coronavirus, J. Virol. 88 (2014) 12,511–12,527.

[25] X.Z. Ma, A. Bartczak, J. Zhang, W. He, I. Shalev, D. Smil, L. Chen, J. Phillips, J.J. Feld, N. Selzner, G. Levy, I. McGilvray, Protein interferon-stimulated gene 15 conjugation delays but does not overcome coronavirus proliferation in a model of fulminant hepatitis, J. Virol. 88 (2014) 6195–6204.

[26] X. Deng, S. Agnihothram, A.M. Mielech, D.B. Nichols, M.W. Wilson, S.E. StJohn, S.D. Larsen, A.D. Mesecar, D.J. Lenschow, R.S. Baric, S.C. Baker, A chimeric virus-mouse model system for evaluating the function and inhibition of papain-like proteases of emerging coronaviruses, J. Virol. 88 (2014) 11,825–11,833.

[27] T.W. James, N. Frias-Staheli, J.-P. Bacik, J.M. Levingston Macleod, M. Khajehpour, A. García-Sastre, B.L. Mark, Structural basis for the removal of ubiquitin and interferon-stimulated gene 15 by a viral ovarian tumor domain-containing protease, Proc. Natl. Acad. Sci. 108 (2011) 2222–2227.

[28] M. Akutsu, Y. Ye, S. Virdee, J.W. Chin, D. Komander, Molecular basis for ubiquitin and ISG15 cross-reactivity in viral ovarian tumor domains, Proc. Natl. Acad. Sci. 108 (2011) 2228–2233.

[29] J. Narasimhan, M. Wang, Z. Fu, J.M. Klein, A.L. Haas, J.-J.P. Kim, Crystal structure of the interferon-induced ubiquitin-like protein ISG15, J. Biol. Chem. 280 (2005) 27,356–27,365.

[30] R. Guan, L.-C. Ma, P.G. Leonard, B.R. Amer, H. Sridharan, C. Zhao, R.M. Krug, G.T. Montelione, Structural basis for the sequence-specific recognition of human ISG15 by the NS1 protein of influenza B virus, Proc. Natl. Acad. Sci. 108 (2011) 13,468–13,473.

[31] C. Zhao, S.L. Beaudenon, M.L. Kelley, M.B. Waddell, W. Yuan, B.A. Schulman, J.M. Huibregtse, R.M. Krug, The UbcH8 ubiquitin E2 enzyme is also the E2 enzyme for ISG15, an IFN-alpha/beta-induced ubiquitin-like protein, Proc. Natl. Acad. Sci. U. S. A. 101 (2004) 7578–7582.

[32] S.D. Speer, Z. Li, S. Buta, B. Payelle-Brogard, L. Qian, F. Vigant, E. Rubino, T.J. Gardner, T. Wedeking, M. Hermann, J. Duehr, O. Sanal, I. Tezcan, N. Mansouri, P. Tabarsi, D. Mansouri, V. Francois-Newton, C.F. Daussy, M.R. Rodriguez, D.J. Lenschow, A.N. Freiberg, D. Tortorella, J. Piehler, B. Lee, A. García-Sastre, S. Pellegrini, D. Bogunovic, ISG15 deficiency and increased viral resistance in humans but not mice, Nat. Commun. 7 (2016) 11,496.

[33] Y.M. Baez-Santos, S.J. Barraza, M.W. Wilson, M.P. Agius, A.M. Mielech, N.M. Davis, S.C. Baker, S.D. Larsen, A.D. Mesecar, X-ray structural and biological evaluation of a series of potent and highly selective inhibitors of human coronavirus papain-like proteases, J. Med. Chem. 57 (2014) 2393–2412.

[34] J.E. Sanchez, P.G. Gross, R.W. Goetze, R.M. Walsh, W.B. Peeples, Z.A. Wood, Evidence of kinetic cooperativity in dimeric ketopantoate reductase from *Staphylococcus aureus*, Biochemistry 54 (2015) 3360–3369.

[35] Z. Otwinowski, W. Minor, Processing of X-ray diffraction data collected in oscillation mode, Methods Enzymol. 276 (1997) 307–326.

[36] A.J. McCoy, R.W. Grosse-Kunstleve, P.D. Adams, M.D. Winn, L.C. Storoni, R.J. Read, Phaser crystallographic software, J. Appl. Crystallogr. 40 (2007) 658–674.

[37] T.C. Terwilliger, R.W. Grosse-Kunstleve, P.V. Afonine, N.W. Moriarty, P.H. Zwart, L.-W. Hung, R.J. Read, P.D. Adams, Iterative model building, structure refinement and density modification with the PHENIX AutoBuild wizard, Acta Crystallogr. Sect. D 64 (2008) 61–69.

[38] P. Emsley, K. Cowtan, Coot: model-building tools for molecular graphics, Acta Crystallogr. Sect. D 60 (2004) 2126–2132.

[39] P.D. Adams, P.V. Afonine, G. Bunkoczi, V.B. Chen, I.W. Davis, N. Echols, J.J. Headd, L.-W. Hung, G.J. Kapral, R.W. Grosse-Kunstleve, A.J. McCoy, N.W. Moriarty, R. Oeffner, R.J. Read, D.C. Richardson, J.S. Richardson, T.C. Terwilliger, P.H. Zwart, PHENIX: a comprehensive Python-based system for macromolecular structure solution, Acta Crystallogr. Sect. D 66 (2010) 213–221.

[40] V.B. Chen, W.B. Arendall III, J.J. Headd, D.A. Keedy, R.M. Immormino, G.J. Kapral, L.W. Murray, J.S. Richardson, D.C. Richardson, MolProbity: all-atom structure validation for macromolecular crystallography, Acta Crystallogr. Sect. D 66 (2010) 12–21.

[41] T.J. Dolinsky, J.E. Nielsen, J.A. McCammon, N.A. Baker, PDB2PQR: an automated pipeline for the setup of Poisson-Boltzmann electrostatics calculations, Nucleic Acids Res. 32 (2004) W665–W667.